Pergamon

Int. J. Solids Structures Vol. 33, No. 20–22, pp. 2899–2938, 1996

0020–7683/96 $15.00 + .00

PII: S0020–7683(95)00255–3

COMPUTATIONAL MODELLING OF IMPACT DAMAGE IN BRITTLE MATERIALS

G. T. CAMACHO* and M. ORTIZ†
Division of Engineering, Brown University, Providence, RI 02912, U.S.A.

Abstract—A Lagrangian finite element method of fracture and fragmentation in brittle materials is developed. A cohesive-law fracture model is used to propagate multiple cracks along arbitrary paths. In axisymmetric calculations, radial cracking is accounted for through a continuum damage model. An explicit contact/friction algorithm is used to treat the multi-body dynamics which inevitably ensues after fragmentation. Rate-dependent plasticity, heat conduction and thermal coupling are also accounted for in calculations. The properties and predictive ability of the model are exhibited in two case studies: spall tests and dynamic crack propagation in a double cantilever beam specimen. As an example of application of the theory, we simulate the experiments of Field (1988) involving the impact of alumina plates by steel pellets at different velocities. The calculated conical, lateral and radial fracture histories are found to be in good agreement with experiment.

1. INTRODUCTION

The response of brittle materials to impact loading has been extensively investigated experimentally (Shockey *et al.*, 1974; Grady and Kipp, 1979; Ahrens and Rubin, 1993; Lankford, 1977, 1983; Longy and Cagnoux, 1989; Espinosa *et al.*, 1992; Shockey *et al.*, 1990a; Woodward *et al.*, 1994). In particular, particle impact studies (Bowden and Field, 1964; Field, 1971, 1988; Tsai and Kolsky, 1967; Arbiter, 1969; Cherepanov and Sokolinsky, 1972; Evans *et al.*, 1977, 1978; Knight *et al.*, 1977; Shockey *et al.*, 1990b), in which, typically, a metallic pellet strikes a glass, ceramic or rock plate, provide a means of identifying the failure modes of projectile and target for a wide range of impact velocities. Specimens and pellets undergo inelastic deformations and sustain damage ranging in severity from surface cracks at low impact velocities, variously developed conical, lateral and radial fractures at intermediate speeds, and catastrophic fragmentation at sufficiently high velocities.

By way of contrast, the assessment of impact performance of brittle materials by computer simulation remains an elusive goal. Current models are, for the most part, based on continuum damage theories in which the net effect of fracture is idealized as a degradation of the elasticity of the material (Seaman *et al.*, 1985; Curran *et al.*, 1987, 1993; Walter, 1992; Johnson *et al.*, 1992; Rajendran, 1994). In addition, fragmentation has often been modelled by recourse to global energy balance concepts (Grady and Kipp, 1993). However, continuum theories of fracture and fragmentation suffer from obvious shortcomings. Thus, the discrete nature of cracks is lost in these theories. In homogeneizing a cracked solid, sweeping assumptions must necessarily be made regarding the distribution and geometry of the cracks, which at best are described by a few state variables, and their interactions. The determination of the effective properties of a cracked solid under dynamic conditions presents additional difficulties stemming from the finite speed at which signals propagate between cracks (Freund, 1990). However, perhaps the most fundamental objection to continuum theories is that the failure of a brittle specimen is frequently governed by the growth of a single dominant crack, a situation which is not amenable to homogeneization.

* Present address: Hibbitt, Karlsson and Sorensen, Inc., Pawtucket, RI 02860, U.S.A.
† Present address: Graduate Aeronautical Laboratories, California Institute of Technology, Pasadena, CA 91125, U.S.A.

In this paper, we depart from continuum damage theories and investigate the feasibility of accounting explicitly for individual cracks as they nucleate, propagate, branch and possibly link up to form fragments. Cracks are allowed to form and propagate along element boundaries in accordance with a cohesive-law model (Ortiz and Suresh, 1993; Xu and Needleman, 1994). Clearly, it is incumbent upon the mesh to provide a rich enough set of possible fracture paths, an issue which we address within the framework of adaptive meshing. In contrast to other approaches (Ortiz and Suresh, 1993; Xu and Needleman, 1994) which require interfacial elements to be inserted at the outset along potential fracture paths, we adaptively create new surfaces as required by the cohesive model by duplicating nodes along previously coherent element boundaries. The cohesive fracture model and its finite element implementation are discussed in Section 7.

In cases in which profuse cracking takes place, fractures inevitably intersect to form discrete fragments. The complicated arrangements of bodies and boundaries which arise can be conveniently described hierarchically as discussed in Section 2. If the extent of fragmentation is sufficiently severe, the comminuted phase flows as a granular material. Under these conditions, the multiple collisions and frictional interactions between the fragments have to be monitored efficiently. In particular, the large number of simultaneous contacts requires the contact search algorithm to be optimized for computational efficiency. Algorithmically demanding contact situations, such as those involving sharp portions of fragment surfaces, occur with some frequency and need to be resolved expediently. The contact/friction algorithm employed in calculations is described in Section 4.

While the methodology developed here applies equally in two and three dimensions, the scale of the calculations can be reduced considerably in problems possessing axial symmetry, e.g., normal impact by a solid of revolution. If the calculations are restricted to a meridional plane, thereby effecting a much desirable reduction in dimensionality, radial cracks can no longer be monitored explicitly and have to be modelled in a continuum sense. The computational pay-off in these cases is considerable enough that, by way of compromise, we adopt a hybrid formulation in which conical and lateral cracks are modelled discretely while radial cracks are modelled continuously.

Under severe conditions, the projectile and the target can undergo extensive plastic deformations and temperature rises. A sizeable fraction of the plastic work is converted into heat, which is also generated at frictional contacts. The mechanical and thermal equations are fully coupled as a consequence of thermal softening. The integration of the coupled thermo-mechanical equations is discussed in Section 5. Damage and plasticity may also be expected to be coupled, as the presence of microcracks introduces local stress concentrations which may in turn drive plastic deformation. Additionally, the pressures under the impactor can rise to very high values. Under these conditions, the conventional flow theories of plasticity have to be augmented by a suitable equation of state for the volumetric response. The constitutive framework adopted in calculations is described in Section 6. A related endeavor concerns the development of robust finite elements which retain adequate performance under extreme conditions of pressure and deformation. Matters of finite element design are briefly addressed in Section 2.

We have validated and calibrated the theory by simulating standard spall and double cantilever tests in some detail. The results are collected in Section 8. As an application of the theory, in Section 9 we present simulations of the pellet–plate impact experiments of Field (1988). The insights revealed by these tests as regards the predictive ability and limitations of the theory are briefly discussed in Section 10.

2. SYSTEM REPRESENTATION

In a typical impact event, the computational model originally comprises a small collection of intact bodies. However, after extensive fracture and fragmentation, the system may come to be composed of a multitude of interacting fragments. Indeed, in the simulations envisioned here the fragments can readily number in the thousands. Evidently, an efficient data structure needs to be designed for organizing and processing all the elements of the model. Our approach is similar in spirit to the discrete element method (Cundall and Hart,

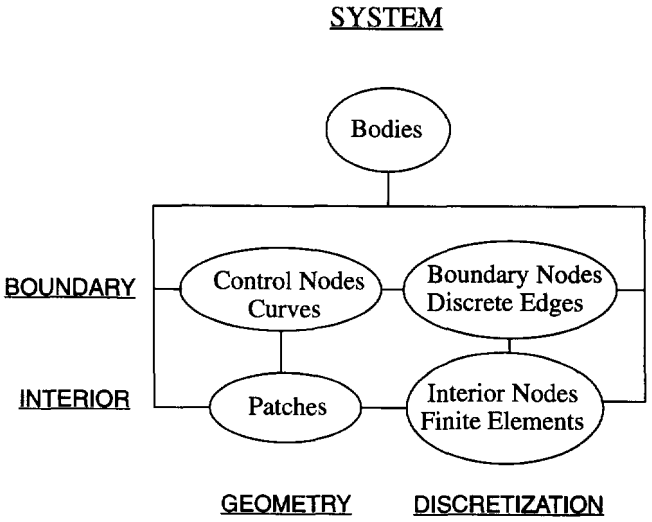

Fig. 1. System hierarchy.

1992; Hocking, 1992), and allows the number of cracks and fragments to proliferate without any bounds other than the limit to refinement imposed by the available computing resources.

The system hierarchy adopted is shown in Fig. 1. As in other modelling approaches (Baehmann *et al.*, 1987; Peraire *et al.*, 1987; Jin and Wiberg, 1990) the aim is to first define the model geometry simply and subsequently discretize it into finite elements. At the top level, the hierarchy comprises a set of bodies. A body in turn comprises a boundary and an interior. In a two-dimensional context, each body is regarded as a patch bounded by boundary curves. These curves are in turn defined by control nodes. The boundary of the patch is composed of both exterior and interior surfaces. The latter may arise as cracks nucleate in the interior of the body. The boundary is discretized into edges defined by boundary nodes. The interior of the body is discretized into finite elements. In subsequent developments we distinguish between exterior and interior nodes. Exterior or boundary nodes are those which lie on the current boundary of the body. The remaining nodes are identified as interior to the body. An example of the geometry and discretization of a system is shown in Fig. 2.

The advancing front automatic mesh generation algorithm is employed to discretize each patch into triangular finite elements from boundary information (Peraire *et al.*, 1987; Jin and Wiberg, 1990). The minimal amount of input data required renders the method particularly attractive. The advancing front algorithm uses boundary nodes to define an initial front from which interior nodes and elements are simultaneously generated. The boundary information required by the advancing front method is also useful for defining contact surfaces. In this context, the creation of cracks involves the modification of the boundary edge and node information, followed by the addition of new bodies to the system if complete fragmentation occurs. Continuous maintenance and tracking of the evolving boundary and interior ensure the integrity of the system data structure throughout the analysis.

The ability to construct meshes by triangulations simply and automatically provides an incentive for the use of triangular elements. In applications such as envisioned here, triangular elements offer the additional advantage of furnishing more potential fracture surfaces than quadrilateral elements. First-order triangular elements suffer from volumetric and shear locking which can result in gross inaccuracies (Nagtegaal *et al.*, 1974), unless meshed in a cross-triangle configuration. However, this configuration is generally incompatible with the unstructured meshes considered here. By contrast, six-noded elements with linear strain interpolation do not lock (Hughes, 1987). In addition, the presence of midside nodes in the six-node triangular element facilitates the initiation of interior cracks, as discussed in Section 7.1.

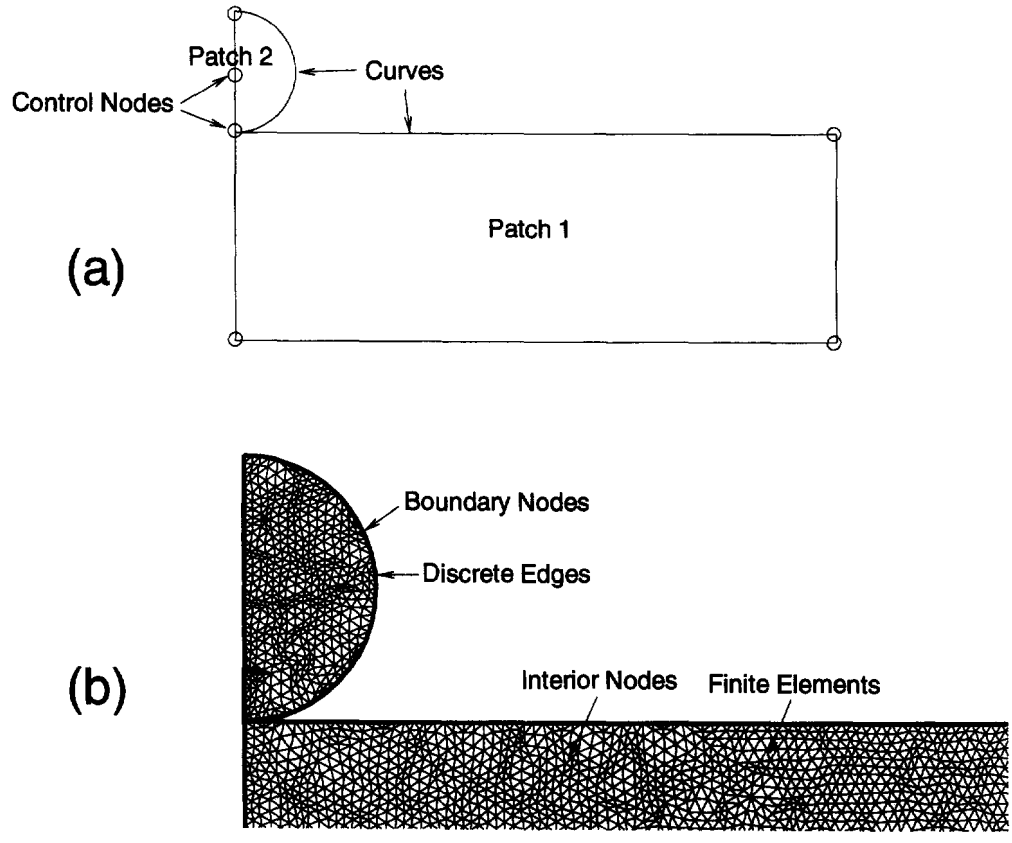

Fig. 2. Example of system geometry and discretization.

Unfortunately, off-the-shelf Lagrangian six-noded elements give rise to unbalanced midside and corner reactions bearing a 2:1 ratio in regular meshes subjected to uniform tractions, and the elements tend to perform poorly under severe impact conditions. Similar pathologies afflict the lumped mass matrix. To sidestep these difficulties, we use an assumed strain six-noded triangular element with linear stress and strain interpolation which is free of volumetric locking while yielding balanced midside and corner reactions and masses in the natural ratio of 1:1 (Camacho, 1996). This ensures, for instance, that a uniform acceleration is imparted to the nodes at the contact between a uniformly meshed straight-sided body and a flat rigid plate, a clearly desirable attribute.

3. EQUATIONS OF MOTION

Consider a body initially occupying a reference configuration B_0, and a process of incremental loading whereby the deformation mapping over B_0 changes from $\boldsymbol{\phi}_n$, at time t_n, to $\boldsymbol{\phi}_{n+1} = \boldsymbol{\phi}_n + \mathbf{u}$, at time $t_{n+1} = t_n + \Delta t$. Dynamic equilibrium is enforced at time t_{n+1} weakly by recourse to the virtual work principle

$$\int_{B_0} \mathbf{P}_{n+1} : \nabla_0 \boldsymbol{\eta} \, \mathrm{d}V_0 - \int_{B_0} (\mathbf{f}_{n+1} + \rho_0 \mathbf{a}_{n+1}) \cdot \boldsymbol{\eta} \, \mathrm{d}V_0 - \int_{\partial B_{0\sigma}} \mathbf{t}_{n+1} \cdot \boldsymbol{\eta} \, \mathrm{d}S_0 = 0 \tag{1}$$

where $\mathbf{P}_{n+1}$ denotes the first Piola–Kirchhoff stress field at time t_{n+1}, $\mathbf{f}_{n+1}$, $\mathbf{a}_{n+1}$ and $\mathbf{t}_{n+1}$ are the corresponding body forces, accelerations and boundary tractions, respectively, ρ_0 is the mass density on the reference configuration, $\boldsymbol{\eta}$ is an admissible virtual displacement field, and ∇_0 denotes the material gradient. Upon discretization of (1) with finite elements the governing equations become

$$\mathbf{M}\mathbf{a}_{n+1} + \mathbf{F}^{int}_{n+1} = \mathbf{F}^{ext}_{n+1} \tag{2}$$

where $\mathbf{M}$ is a lumped mass matrix, $\mathbf{F}^{ext}$ is the external force array including body forces and surface tractions and $\mathbf{F}^{int}$ is the internal force array arising from the current state of stress.

The second-order accurate central difference scheme is used to discretize (2) in time (Hughes, 1987; Hughes and Belytschko, 1983; Belytschko, 1983), with the result

$$\mathbf{d}_{n+1} = \mathbf{d}_n + \Delta t \mathbf{v}_n + \tfrac{1}{2}\Delta t^2 \mathbf{a}_n \tag{3}$$

$$\mathbf{a}_{n+1} = \mathbf{M}^{-1}(\mathbf{F}^{ext}_{n+1} - \mathbf{F}^{int}_{n+1}) \tag{4}$$

$$\mathbf{v}_{n+1} = \mathbf{v}_n + \tfrac{1}{2}\Delta t(\mathbf{a}_{n+1} + \mathbf{a}_n) \tag{5}$$

where **d**, **v** and **a** denote the displacement, velocity and acceleration arrays, respectively. Explicit integration is particularly attractive in impact problems, since the resolution of the various waves in the solution necessitates the use of small time steps well under the stability limit (Hughes, 1983). In addition, explicit contact algorithms are more robust and straightforward than their implicit counterparts, a distinct advantage in problems involving fragmentation where complicated contact situations inevitably arise. Explicit integration is also advantageous in three-dimensional calculations, where implicit schemes lead to system matrices which often exceed the available in-core storage capacity. Yet another desirable aspect of explicit algorithms is that they are ideally suited for concurrent computing (Mathur *et al.*, 1993).

4. CONTACT

In the applications of interest here, complicated contact situations develop which involve multiple collisions between deformable bodies as well as self-contact across crack surfaces. We have found the contact algorithm developed by Taylor and Flanagan (1987) for the PRONTO2D explicit dynamics code particularly effective in dealing with such complex contact situations. In this approach, the bodies in contact can be deformable or rigid. The contacting surfaces are designated as master and slave. A balanced master-slave approach in which surfaces alternately act as master and slave is employed. However, rigid surfaces are always treated as master surfaces.

The method starts with the calculation of predictor nodal positions, velocities and accelerations $\mathbf{x}^{pred}_{n+1}$, $\mathbf{v}^{pred}_{n+1}$ and $\mathbf{a}^{pred}_{n+1}$, respectively, assuming that no contact has occurred. A predictor configuration where penetration has occurred is sketched in Fig. 3a. In enforcing the contact conditions, it proves convenient to introduce an auxiliary consecutive numbering of the nodes on the contacting surfaces. The penetration distances $\delta_{s,j}$ for all nodes j on the slave surface are then determined on the predictor configuration. Here and henceforth, labels m and s are used to designate the master and slave surfaces, respectively. The contact

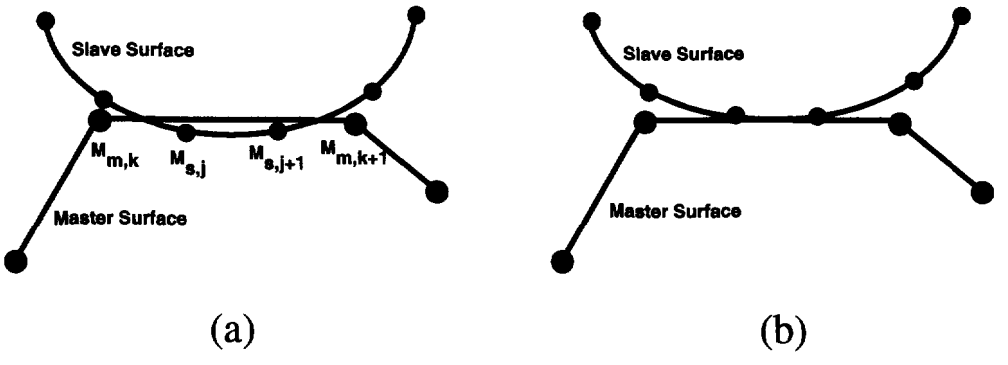

Fig. 3. (a) Predictor configuration of surfaces. (b) Kinematically compatible surfaces.

forces required to prevent penetration, were the master surface to remain stationary at the predictor configuration, are given by:

$$P_{s,j} = \frac{2M_{s,j}\,\delta_{s,j}}{\Delta t^2} \tag{6}$$

where $M_{s,j}$ is the mass of node j on the slave surface. Next, normal acceleration corrections are introduced which eliminate the unwanted penetration, Fig. 3b. The requisite accelerations are

$$a_{m,k}^{corr} = \frac{\sum_j (\omega_{s\to m,j} P_{s,j})}{M_{m,k} + \sum_j (\omega_{s\to m,j} M_{s,j})}, \tag{7}$$

$$a_{s,j}^{corr} = \sum_k (\omega_{m\to s,k} a_{m,k}^{corr}) - \frac{P_{s,j}}{M_{s,j}} \tag{8}$$

where $\omega_{s\to m,j}$ and $\omega_{m\to s,k}$ are weights dependent on position. A Coulomb friction model is also adopted from Taylor and Flanagan (1987). Let $\mathbf{t}$ represent the unit tangent to the master segment. The tangential component of the relative predictor velocity between the slave node and the master segment is then given by

$$\Delta v_{s,j} = \mathbf{t} \cdot \left(\mathbf{v}_{s,j}^{pred} - \sum_k \omega_{m\to s,k} \mathbf{v}_{m,k}^{pred} \right). \tag{9}$$

The force that must be applied to the slave node to cancel its relative tangential velocity, i.e., to produce perfect stick, is

$$F_{s,j}^{stick} = -\frac{M_{s,j}\Delta v_{s,j}}{\Delta t}. \tag{10}$$

The tangential force exerted by the master surface on a slave node cannot exceed the maximum frictional resistance

$$F_{s,j} = \frac{F_{s,j}^{stick}}{|F_{s,j}^{stick}|} \min\left(\mu N_{s,j}, |F_{s,j}^{stick}|, F_{shearlimit}\right) \tag{11}$$

where $F_{shearlimit}$ accounts for the shear strength of the material and $N_{s,j}$ is the normal contact force given by

$$N_{s,j} = M_{s,j} a_{s,j}^{corr} \cdot \mathbf{n}. \tag{12}$$

Here $\mathbf{n}$ is the unit normal to the surface. The tangential force induces the tangential acceleration corrections

$$a_{s,j}^{corr} = \frac{F_{s,j}}{M_{s,j}} \tag{13}$$

$$a_{m,k}^{corr} = -\frac{\sum_j \omega_{s\to m,j} F_{s,j}}{M_{m,k}}. \tag{14}$$

This completes the computation of the acceleration array. The corresponding displacement and velocity corrections follow from (3) and (5).

The procedure just outlined tacitly presumes that the master segment which is penetrated by each slave node during the time step is known. Because of the large number of potential contacts, however, the evaluation of the contact conditions is a non-trivial task which can be broken down into two steps: the contact search and the contact logic. For every slave node, the contact search determines the set of nearest master nodes. On the basis of this nearest-neighbor set, the contact logic subsequently determines the actual master segment contacted by the slave node.

The exhaustive search of all master nodes constitutes an $O(N^2)$ operation, where N is the number of contact nodes. This operation count can be substantially improved for large N (Hallquist *et al.*, 1985; Taylor and Flanagan, 1987; Zhong and Nilsson, 1990). Quadtree searches (e.g., Lohner, 1988) are particularly effective for this purpose. The method requires the master nodes to be arranged as a quadtree. Each level of the quadtree corresponds to a partition of the contact nodes into four subdomains. The leaves of the tree consist of domains containing at most four nodes. For each slave node, a quadtree search is then performed which returns the N_{near} nearest master nodes. The appropriate value of N_{near} depends on the relative sizes of the master and slave elements. The nearest-neighbor sets are stored for subsequent use. The quadtree search is an $O(N \log(N))$ operation which is performed only when the boundary state changes. This may occur due to the creation of new crack nodes or when the contact logic detects contact with a master segment close to the end of the nearest-neighbor set. The frequency of the quadtree searches is diminished by the choice of a large N_{near}, but these gains occur at the expense of a higher storage requirement. The optimal choice of N_{near} therefore involves a memory-computational time tradeoff.

For each slave node, the contact logic operation leading to the detection of active contacts is performed on the N_{near} nearest master nodes only. We follow the contact logic developed by Taylor and Flanagan (1987), which may be consulted for specifics. In our simulations however, situations frequently arise in which a number of sharp edges simultaneously come into contact, Fig. 4. In order to resolve these situations, we have augmented the contact logic of Taylor and Flanagan (1987)—at some loss of computational efficiency—by performing segment intersection calculations and by detecting instances in

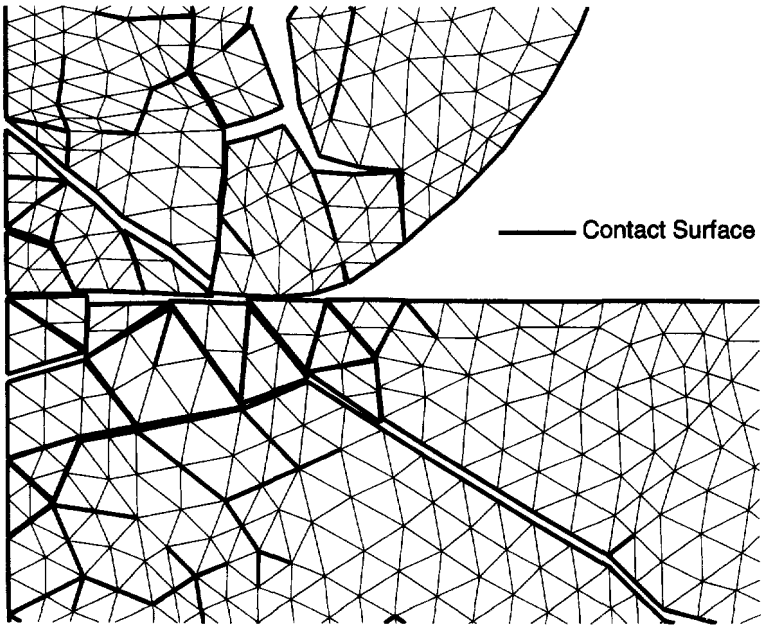

Fig. 4. Example of multi-bodies and their contact surfaces.

which, owing to a breakdown in the basic contact logic rules, a slave node strays into the interior of a master element.

5. THERMAL EFFECTS

In the course of an impact event, substantial amounts of heat may be generated due to the plastic working of the solid and friction at the contact surfaces. The temperatures attained can be quite high and have a considerable influence on the mechanical response. The relevant balance law to be considered in this case is the heat equation, which can be expressed in weak form as

$$\int_{B_t} \rho c \dot{T} \eta \, \mathrm{d}V + \int_{\partial B_{tq}} h\eta \, \mathrm{d}S = \int_{B_t} \mathbf{q} \cdot \nabla \eta \, \mathrm{d}V + \int_{B_t} s\eta \, \mathrm{d}V \tag{15}$$

where ρ is the current mass density, c the heat capacity, T the spatial temperature field, η an admissible virtual temperature field, h the outward heat flux through the surface, $\mathbf{q}$ is the heat flux, s is the distributed heat source density, and B_{tq} the current Neumann boundary. The main sources of heat in our applications are plastic deformation in the bulk and frictional sliding at the interfaces. The rate of heat supply due to the first is estimated as

$$s = \beta \dot{W}^p \tag{16}$$

where $\dot{W}^p$ is the plastic power per unit deformed volume and the Taylor–Quinney (Taylor and Quinney, 1931) coefficient β is of the order of 0.9 (e.g., Kobayashi *et al.*, 1989). The rate at which heat is generated at the frictional contact, on the other hand, is

$$h = \mathbf{t} \cdot [\![\mathbf{v}]\!] \tag{17}$$

where $\mathbf{t}$ is the contact traction and $[\![\mathbf{v}]\!]$ is the jump in velocity across the contact. This heat must be apportioned between the bodies. Using transient half-space solutions, the ratio of the heat supply to body 1, h_1, and body 2, h_2 can be computed as (Marusich and Ortiz, 1994)

$$\frac{h_1}{h_2} = \frac{\sqrt{k_1 \rho_1 c_1}}{\sqrt{k_2 \rho_2 c_2}} \tag{18}$$

where k_α, ρ_α and c_α, $\alpha = 1, 2$, are the thermal conductivity, mass density and heat capacity of the contacting bodies.

Inserting the finite element interpolation into (15) results in the semi-discrete system of equations (Belytschko, 1983)

$$\mathbf{C}\dot{\mathbf{T}} + \mathbf{K}\mathbf{T} = \mathbf{Q} \tag{19}$$

where $\mathbf{T}$ is the array of nodal temperatures, $\mathbf{C}$ is the heat capacity matrix, $\mathbf{K}$ is the conductivity matrix, and $\mathbf{Q}$ is the heat source array. In the applications of interest here, the mechanical equations always set the critical time step for stability. It therefore suffices to lump the capacitance matrix and integrate the energy eqn (19) explicitly by the forward Euler algorithm (Hughes, 1987; Hughes and Belytschko, 1983; Belytschko, 1983), with the result

$$\mathbf{T}_{n+1} = \mathbf{T}_n + \Delta t \dot{\mathbf{T}}_n \tag{20}$$

$$\mathbf{C}\dot{\mathbf{T}}_n + \mathbf{K}_n \mathbf{T}_n = \mathbf{Q}_n. \tag{21}$$

A staggered procedure (Park and Felippa, 1983) is adopted for the purpose of coupling

the thermal and mechanical equations. Mechanical and thermal computations are staggered assuming constant temperature during the mechanical step and constant heat generation during the thermal step. Following Lemonds and Needleman (1986), a mechanical step is taken first based on the current distribution of temperatures, and the heat generated is computed from (16) and (17). The heat thus computed is used in the thermal analysis where temperatures are recomputed by recourse to the forward Euler algorithm (20) and (21). The resulting temperatures are then used in the mechanical step and incorporated into the thermal-softening model described in Section 6, which completes one time-stepping cycle. A flowchart of the staggered procedure is shown in Box 1.

(i) Initialize $\mathbf{T}_1 = \mathbf{T}_0 + \Delta t \dot{\mathbf{T}}_0$, $n = 0$.
(ii) Isothermal mechanical step:

$$\{\mathbf{x}_n, \mathbf{v}_n, \mathbf{a}_n, \mathbf{T}_{n+1}\} \rightarrow \{\mathbf{x}_{n+1}, \mathbf{v}_{n+1}, \mathbf{a}_{n+1}, \mathbf{T}_{n+1}\}$$

(iii) Heat generation (bulk + contact)
(iv) Rigid conductor step:

$$\{\mathbf{x}_{n+1}, \mathbf{v}_{n+1}, \mathbf{a}_{n+1}, \mathbf{T}_{n+1}\} \rightarrow \{\mathbf{x}_{n+1}, \mathbf{v}_{n+1}, \mathbf{a}_{n+1}, \mathbf{T}_{n+2}\}$$

(v) $n \rightarrow n+1$, GOTO (ii).

Box 1. Staggered procedure for thermo-mechanical coupling.

6. CONSTITUTIVE MODEL

During impact events, materials frequently experience considerable volumetric and shear deformations. The volumetric or dilatational response is presumed to be governed by an equation of state while the shear or deviatoric response is assumed to obey a conventional flow theory of plasticity. We begin by decomposing the Cauchy stress tensor into hydrostatic and deviatoric components,

$$\sigma_{ij} = -p\,\delta_{ij} + s_{ij}, \tag{22}$$

where p is the hydrostatic pressure and s_{ij} is the stress deviator.

We adopt an equation of state of the Mie–Gruneisen type,

$$p = (K_1\mu + K_2\mu^2 + K_3\mu^3)(1 - \tfrac{1}{2}\Gamma\mu) + \Gamma\rho e, \tag{23}$$

where $\mu = J^{-1} - 1$, $J = \det \mathbf{F} = \rho_0/\rho$ is the Jacobian of the deformation, $\mathbf{F}$ is the deformation gradient, ρ is the current mass density, e is the internal energy per unit mass, Γ is the Gruneisen coefficient and K_1, K_2 and K_3 are material coefficients. In addition, a small artificial bulk viscosity is introduced to prevent high velocity gradients from collapsing elements and to quiet down ringing (Taylor and Flanagan, 1987). The viscous pressure takes the form

$$q = b_1 \rho c_d l \frac{\dot{J}}{J} - \rho\left(b_2 l \frac{\dot{J}}{J}\right)^2 \tag{24}$$

where b_1 and b_2 are constants, c_d is the dilatational wave speed, $\dot{J}/J$ is the volumetric strain rate and l is a typical element dimension. The principle of conservation of energy requires the increase in internal energy of any subbody to equal to the sum of the work of deformation and the heat input into the subbody, leading to the identity

$$\rho\dot{e} = \sigma_{ij}d_{ij} + \rho c\dot{T} \tag{25}$$

where $d_{ij} = (v_{i,j}+v_{j,i})/2$ is the rate of deformation tensor. In calculations, we update the pressure and the internal energy by recourse to the integration scheme developed by Taylor and Flanagan (1987).

For the deviatoric response we adopt a standard formulation of finite deformation plasticity based on a multiplicative decomposition of the deformation gradient into elastic and plastic components. We employ the fully implicit algorithm of Cuitiño and Ortiz (1992) for performing the constitutive updates. In a typical impact penetration event, very high strain rates in excess of $10^5\ s^{-1}$ may be attained. Under these conditions, a power viscosity law with constant rate sensitivity m is not adequate. Indeed, the experimental stress–strain rate curves for ceramics (Lankford, 1977, 1983; Steinberg, 1991) and metals (Klopp *et al.*, 1985; Clifton and Klopp, 1985; Zhou *et al.*, 1992) exhibit a transition at strain rates of the order of 10^3–$10^6\ s^{-1}$ from low to high rate sensitivity. At low strain rates, a rate sensitivity exponent in the range 40–100 adequately fits the data, while in the high strain rate regime a much lower rate sensitivity exponent in the range 4–20 applies. A simple model which accounts for this behavior consists of assuming a stepwise variation of the rate sensitivity exponent m while maintaining continuity of stress (Marusich and Ortiz, 1994). This leads to the relation

$$\left(1+\frac{\dot{\varepsilon}_p}{\dot{\varepsilon}_0^p}\right) = \left(\frac{\bar{\sigma}}{g(\varepsilon_p)}\right)^{m_1}, \quad \text{if} \quad \dot{\varepsilon}^p \leqslant \dot{\varepsilon}_t \tag{26}$$

$$\left(1+\frac{\dot{\varepsilon}^p}{\dot{\varepsilon}_0^p}\right)\left(1+\frac{\dot{\varepsilon}_t}{\dot{\varepsilon}_0^p}\right)^{m_2/m_1-1} = \left(\frac{\bar{\sigma}}{g(\varepsilon^p)}\right)^{m_2}, \quad \text{if} \quad \dot{\varepsilon}^p > \dot{\varepsilon}_t \tag{27}$$

where $\bar{\sigma}$ is the effective Mises stress, g the flow stress, ε^p the accumulated plastic strain, $\dot{\varepsilon}_0^p$ a reference plastic strain rate, m_1 and m_2 are low and high strain rate sensitivity exponents, respectively, and $\dot{\varepsilon}_t$ is the threshold strain rate which separates the two regimes. In calculations, we begin by computing $\dot{\varepsilon}^p$ according to (26), and switch to (27) if the result lies above $\dot{\varepsilon}_t$.

Following Lemonds and Needleman (1986), we also adopt a power hardening law with linear thermal softening. This gives

$$g = \sigma_y[1-\alpha(T-T_0)]\left(1+\frac{\varepsilon^p}{\varepsilon_0^p}\right)^{1/n} \tag{28}$$

where n is the hardening exponent, T the current temperature, T_0 a reference temperature, α the thermal softening coefficient, and σ_y is the yield stress at T_0. It should be noted that, owing to the staggered integration of the coupled thermal–mechanical equations, the temperature T remains fixed during a mechanical step and, therefore, plays the role of a known parameter during a stress update.

7. FRACTURE

In contrast to past and current approaches to fracture and fragmentation, which have largely been based on continuum theories of damage and fragmentation (Seaman *et al.*, 1985; Curran *et al.*, 1987; Johnson and Holmquist, 1992; Rajendran, 1994; Grady and Kipp, 1993; Longy and Cagnoux, 1989; Espinosa *et al.*, 1992), we *explicitly* follow the initiation and propagation of multiple cracks. These cracks can branch and coalesce and eventually lead to the formation of fragments. The creation of new surface is accomplished by allowing initially coherent element boundaries to open according to a cohesive law which models a gradual loss of strength with increasing separation. The cohesive law determines the work of separation, or fracture energy, required for the complete formation

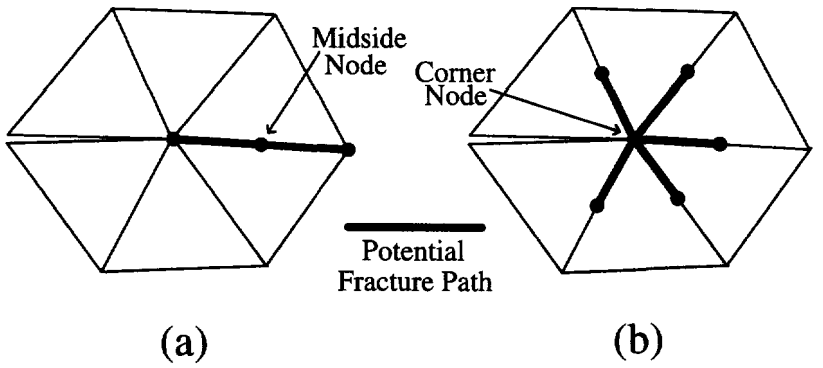

Fig. 5. Potential fracture paths for (a) midside node, and (b) corner node.

of a free surface (Dugdale, 1960; Barrenblatt, 1962; Ortiz, 1988; Ortiz and Suresh, 1993; Xu and Needleman, 1994).

The cracks which result from normal impact by an axisymmetric solid can be classified into two main categories: conical and radial. Conical cracks intersect meridional planes at right angles. We refer to the cracks contained in meridional planes as radial cracks. In order to restrict the calculations to a meridional plane, thereby effecting a much desirable reduction to two spatial dimensions, we develop a hybrid formulation in which conical cracks are modelled discretely by their trace on meridional planes while radial cracks are modelled by a distributed damage model. These aspects of the model are developed in subsequent sections.

7.1. *Conical cracks*

We create new fracture surfaces by splitting nodes according to a brittle fracture criterion. Midside nodes can only be split in one way, namely along the unique element boundary crossing that node, Fig. 5a. By contrast, interior corner nodes can potentially open up along multiple fracture paths, Fig. 5b, all of which need to be evaluated in turn. To this end, we begin by computing the traction $\mathbf{t}$ acting at the node across all potential fracture surfaces. The details of the calculation are given in Appendix A. The computed tractions are resolved into normal and tangential components σ and τ, respectively, Fig. 6a, b.

Consideration of an effective stress intensity factor for mixed-mode fracture (Margolin, 1984; Dienes, 1986) leads to the fracture criteria

$$\sigma^{eff} = \sqrt{\sigma^2 + \beta_\tau \tau^2} \geqslant \sigma_{fr}, \quad \sigma \geqslant 0 \tag{29}$$

$$\sigma^{eff} = \sqrt{\beta_\tau}\langle |\tau| - \mu|\sigma| \rangle \geqslant \sigma_{fr}, \quad \sigma < 0 \tag{30}$$

where β_τ is a shear stress factor, μ is the friction coefficient and σ_{fr} is a fracture stress. In

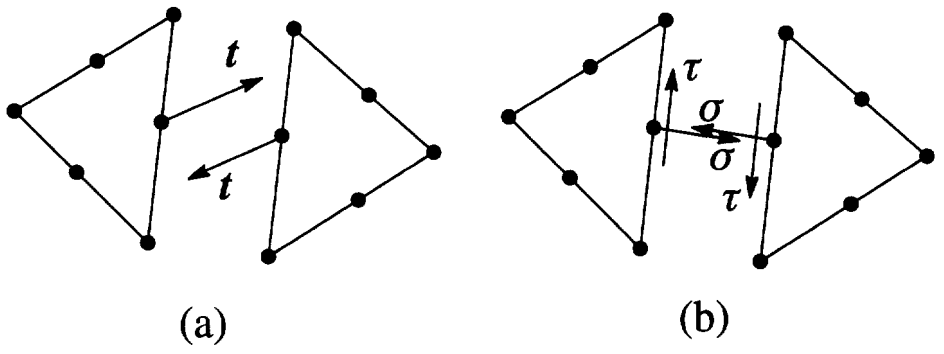

Fig. 6. (a) Midside node traction forces $\mathbf{t}$. (b) Normal and shear stresses σ and τ.

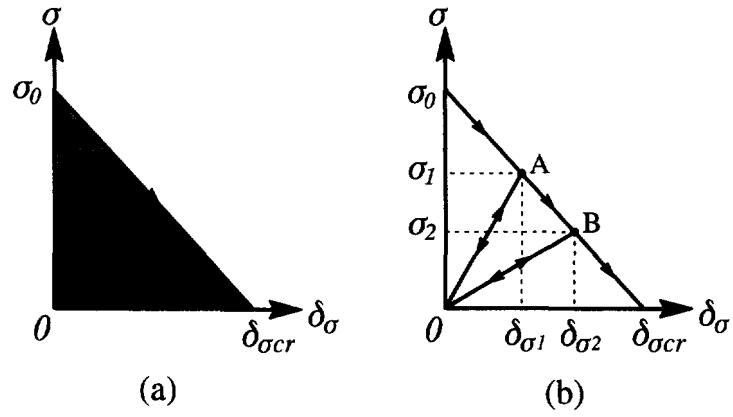

Fig. 7. Tensile cohesive relation.

order to estimate σ_{fr}, we assume that pre-existing flaws populate element boundaries as arrays of collinear slit cracks of half-width a_0. Then σ_{fr} follows from the toughness K_{Ic} of the material as

$$\sigma_{fr} = \frac{K_{Ic}}{\sqrt{\pi a_0}}. \tag{31}$$

When either of the critical conditions (29) or (30) is met, a new surface is introduced into the mesh by suitably doubling nodes.

The cohesive forces which resist the opening and sliding of the new surface are assumed to weaken irreversibly with increasing crack opening displacement, Fig. 7. If the opening velocity changes sign, the cohesive forces are ramped down to zero as the opening displacement itself diminishes to zero, in the spirit of damage mechanics (e.g., Kachanov, 1986). We differentiate between two cases:

1. Tensile case. When the normal opening displacement δ_σ increases monotonically, the cohesive stresses σ and τ are ramped down linearly as a function of δ_σ, Fig. 7a, leading to the relations

$$\sigma = \sigma_0\left(1 - \frac{\delta_\sigma}{\delta_{\sigma cr}}\right) \tag{32}$$

$$\tau = \tau_0\left(\frac{\delta_\sigma}{\delta_{\sigma cr}}\right)\operatorname{sgn}(\delta_\tau) \tag{33}$$

where δ_σ and δ_τ are the normal opening and sliding displacements, respectively, σ_0 and τ_0 are the normal and shear stresses at fracture initiation, respectively, and $\operatorname{sgn}(x) = x/|x|$ is the signum function. The cohesive tractions reduce to zero at the critical opening displacement $\delta_\sigma = \delta_{\sigma cr}$. The new surface is then fully formed and the cohesive tractions vanish thereafter. The area under the tensile cohesive law, $G_c = \sigma_0\,\delta_{\sigma cr}/2$, is the fracture energy measured in fracture tests. If, after some opening displacement $\delta_{\sigma_1} < \delta_{\sigma cr}$ the crack begins to close, the tractions obey the linear unloading relation

$$\sigma = \sigma_0\left(1 - \frac{\delta_{\sigma_1}}{\delta_{\sigma cr}}\right)\frac{\delta_\sigma}{\delta_{\sigma_1}} \tag{34}$$

$$\tau = \tau_0\left(1 - \frac{\delta_{\sigma_1}}{\delta_{\sigma cr}}\right)\frac{\delta_\sigma}{\delta_{\sigma_1}}\,\mathrm{sgn}\,(\delta_\tau) \tag{35}$$

as shown in Fig. 7b. If the crack reopens, the unloading path is reversed up to δ_{σ_1} and, subsequently, the monotonic cohesive relations (32) and (33) are followed.

2. Compressive case. If the tangential displacement δ_τ increases monotonically in magnitude, the cohesive shear stress τ is ramped down linearly according to the relation

$$\tau = \tau_0\left(1 - \frac{|\delta_\tau|}{\delta_{\tau cr}}\right)\mathrm{sgn}\,(\delta_\tau) \tag{36}$$

where τ_0 is the shear stress at fracture initiation, Fig. 8a. The shear stress τ reduces to zero at the critical sliding displacement $|\delta_\tau| = \delta_{\tau cr}$. The new surface is then presumed fully formed and the cohesive tractions vanish thenceforth. Contrariwise, if the direction of shearing is reversed from a sliding displacement $|\delta_{\tau_1}| < \delta_{\tau cr}$, the shear traction obeys the linear unloading/reloading relation

$$\tau = \tau_0\left(1 - \frac{|\delta_{\tau_1}|}{\delta_{\tau cr}}\right)\frac{\delta_\tau}{|\delta_{\tau_1}|} \tag{37}$$

as shown in Fig. 8b. As in the tensile case, the reloading curve simply retraces the unloading path until it rejoins the monotonic cohesive law (36). Since the crack is closed in the compressive case, contact normal and shear tractions act concurrently with the cohesive shear stress.

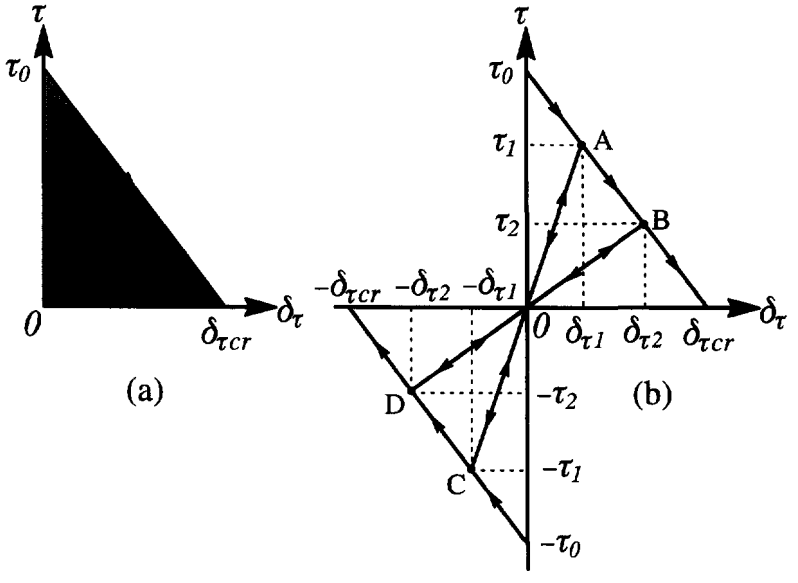

Fig. 8. Shear cohesive relation.

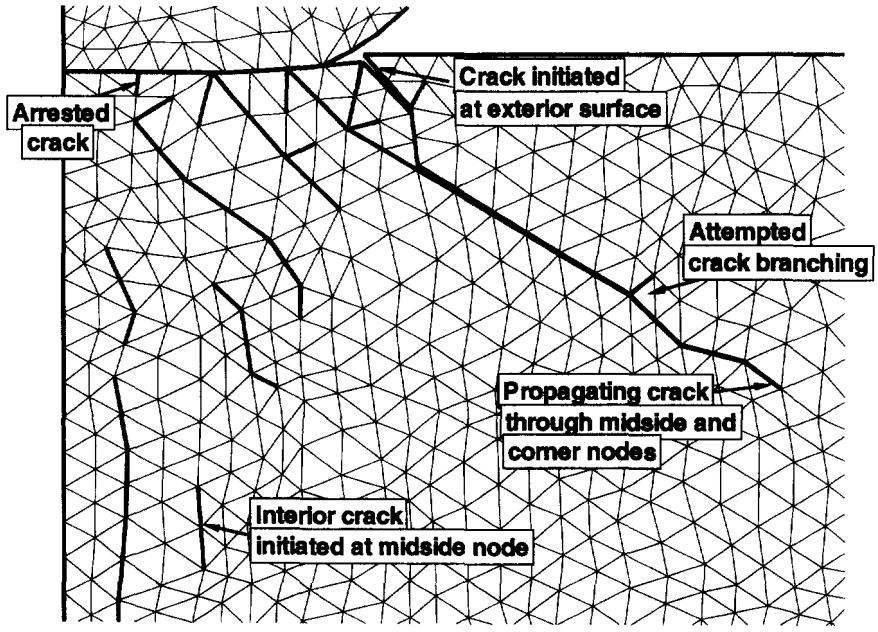

Fig. 9. Crack system.

The crack system of Fig. 9 exemplifies capabilities in our fracture model such as: crack initiation at surfaces and in the interior; and crack propagation, branching and arrest. Additionally, crack closure may result in contact and/or frictional sliding of the crack flanks. The frictional contact conditions resulting from crack closure are enforced with the aid of the contact algorithm discussed in Section 4.

(i) Initialize $k_{body} = 1$.
(ii) Gather list of N_{mid} interior midside nodes of body k_{body} and the elements attached to them. Initialize $k_{mid} = 1$.
(iii) Compute effective stress σ^{eff} at midside node k_{mid}. If $\sigma^{eff} \geqslant \sigma_{fr}$, create a crack by doubling the midside node. At each external corner node connected to the midside node, double the corner node. Perform bookkeeping operations.
(iv) If $k_{mid} < N_{mid}$ then $k_{mid} \to k_{mid}+1$, GOTO (iii).
(v) Gather list of N_{cor} exterior corner nodes of body k_{body} and the elements attached to them. Initialize $k_{cor} = 1$.
(vi) At each interior edge attached to the corner node k_{cor}, compute effective stress σ^{eff} at the corner node. If $\sigma^{eff} \geqslant \sigma_{fr}$, create crack by doubling the corner node. Perform bookkeeping operations.
(vii) If $k_{cor} < N_{cor}$ then $k_{cor} \to k_{cor}+1$, GOTO (vi).
(viii) If $k_{body} < N_{body}$ then $k_{body} \to k_{body}+1$, GOTO (ii).

Box 2. Fracture procedure.

Some issues of implementation are noteworthy. The main steps of the fracture procedure are outlined in Box 2. For modularity and efficiency, each body is processed independently. The fracture criterion is evaluated at all potential crack paths. In particular, at corner nodes all the interior sides of the surrounding elements need to be evaluated. After a crack is created, some bookkeeping operations have to be performed, including (a) storing the cohesive forces for use in the explicit integration procedure in (4), (b) renumbering the nodes of the elements, (c) updating the system information: creating a new body if a new crack splits a current body; updating the discrete edge and boundary node lists. Operations (b) and (c) are necessary to preserve the integrity of the system information.

7.2. *Radial fracture*

We account for conical and lateral cracks explicitly through our fragmentation model. However, in order to keep the calculations axisymmetric, we resort to a continuum damage

model to account for radial cracking. The theory of damage adopted endeavors to represent the weakening effect on the material of nearly co-planar radial microcracks. Fracture patterns of this type can be effectively modelled within the framework of one-dimensional damage theories (Kachanov, 1986; Krajcinovic and Lemaitre, 1987). In addition, the method of extension of Cuitiño and Ortiz (1992) enables the damage model to be conveniently formulated for small strains. We begin by considering the perfectly brittle case and address the issue of elastoplastic coupling subsequently.

Let χ represent the fraction of area which has been fractured on average on a typical meridional plane. The limit of $\chi = 0$ corresponds to the absence of cracking, in which case the stress state is axisymmetric, while the limit $\chi = 1$ represents fully cracked conditions resulting in plane stress behavior. The dependence of the stress–strain relations on the structure parameter χ is postulated to be

$$\sigma_{11} = (\lambda+2\mu)\varepsilon_{11} + \lambda\varepsilon_{22} + \lambda(1-\chi)\varepsilon_{33} \tag{38}$$

$$\sigma_{22} = \lambda\varepsilon_{11} + (\lambda+2\mu)\varepsilon_{22} + \lambda(1-\chi)\varepsilon_{33} \tag{39}$$

$$\sigma_{33} = \lambda(1-\chi)\varepsilon_{11} + \lambda(1-\chi)\varepsilon_{22} + (\lambda+2\mu)(1-\chi)^2\varepsilon_{33} \tag{40}$$

$$\sigma_{12} = 2\mu\varepsilon_{12} \tag{41}$$

$$\sigma_{13} = 2\mu(1-\chi)^2\varepsilon_{13} \tag{42}$$

$$\sigma_{23} = 2\mu(1-\chi)^2\varepsilon_{23} \tag{43}$$

where the third coordinate axis points in the circumferential direction, and λ and μ are the uncracked moduli of the material. As required, in the limit of $\chi \to 0$, (38–43) reduce to axisymmetric stress–strain relations, while in the limit of $\chi \to 1$, (38–43) degenerate to their plane stress counterparts.

Introducing the effective stresses and strains

$$\sigma_{11}^{eff} = \sigma_{11}, \quad \sigma_{22}^{eff} = \sigma_{22}, \quad \sigma_{33}^{eff} = \frac{\sigma_{33}}{1-\chi},$$
$$\sigma_{12}^{eff} = \sigma_{12}, \quad \sigma_{13}^{eff} = \frac{\sigma_{13}}{1-\chi}, \quad \sigma_{23}^{eff} = \frac{\sigma_{23}}{1-\chi} \tag{44}$$

$$\varepsilon_{11}^{eff} = \varepsilon_{11}, \quad \varepsilon_{22}^{eff} = \varepsilon_{22}, \quad \varepsilon_{33}^{eff} = (1-\chi)\varepsilon_{33},$$
$$\varepsilon_{12}^{eff} = \varepsilon_{12}, \quad \varepsilon_{13}^{eff} = (1-\chi)\varepsilon_{13}, \quad \varepsilon_{23}^{eff} = (1-\chi)\varepsilon_{23} \tag{45}$$

eqns (38–43) can be conveniently rewritten as

$$\sigma_{11}^{eff} = (\lambda+2\mu)\varepsilon_{11}^{eff} + \lambda\varepsilon_{22}^{eff} + \lambda\varepsilon_{33}^{eff} \tag{46}$$

$$\sigma_{22}^{eff} = \lambda\varepsilon_{11}^{eff} + (\lambda+2\mu)\varepsilon_{22}^{eff} + \lambda\varepsilon_{33}^{eff} \tag{47}$$

$$\sigma_{33}^{eff} = \lambda\varepsilon_{11}^{eff} + \lambda\varepsilon_{22}^{eff} + (\lambda+2\mu)\varepsilon_{33}^{eff} \tag{48}$$

$$\sigma_{12}^{eff} = 2\mu\varepsilon_{12}^{eff} \tag{49}$$

$$\sigma_{13}^{eff} = 2\mu\varepsilon_{13}^{eff} \tag{50}$$

$$\sigma_{23}^{eff} = 2\mu\varepsilon_{23}^{eff}. \tag{51}$$

Thus, the stress–strain relations are identical to those of an uncracked solid when expressed in terms of effective stresses and strains. In matrix notation,

$$\boldsymbol{\varepsilon}^{eff} = \mathbf{B}(\chi)\boldsymbol{\varepsilon}, \quad \boldsymbol{\sigma}^{eff} = \mathbf{B}^{-T}(\chi)\boldsymbol{\sigma}, \quad \boldsymbol{\sigma}^{eff} = \mathbf{C}\boldsymbol{\varepsilon}^{eff} \tag{52}$$

where $\mathbf{C}$ is the matrix of uncracked elastic moduli. From these definitions, the stress–strain relations may be written in physical variables in the form

$$\boldsymbol{\sigma} = \mathbf{C}^{eff}(\chi)\boldsymbol{\varepsilon} \tag{53}$$

where

$$\mathbf{C}^{eff}(\chi) = \mathbf{B}^{\mathrm{T}}(\chi)\mathbf{C}\mathbf{B}(\chi) \tag{54}$$

are the effective moduli of the cracked solid.

The strain energy of the solid follows as

$$W(\boldsymbol{\varepsilon}, \chi) = \tfrac{1}{2}\boldsymbol{\varepsilon}^{eff} \cdot \mathbf{C} \cdot \boldsymbol{\varepsilon}^{eff} = \tfrac{1}{2}\boldsymbol{\varepsilon} \cdot \mathbf{C}^{eff} \cdot \boldsymbol{\varepsilon}. \tag{55}$$

The free energy is obtained by adding to (55) the surface energy, with the result

$$F(\boldsymbol{\varepsilon}, \chi) = W(\boldsymbol{\varepsilon}, \chi) + \frac{G_c}{l}\chi \tag{56}$$

where l is a material property defining the distance between potential meridional cracking planes (Fig. 10) and G_c is the fracture energy. The driving force for cracking is

$$J = -\frac{\partial F(\boldsymbol{\varepsilon}, \chi)}{\partial \chi} = -\frac{\partial W(\boldsymbol{\varepsilon}, \chi)}{\partial \chi} - \frac{G_c}{l}. \tag{57}$$

A simple kinetic equation for χ is

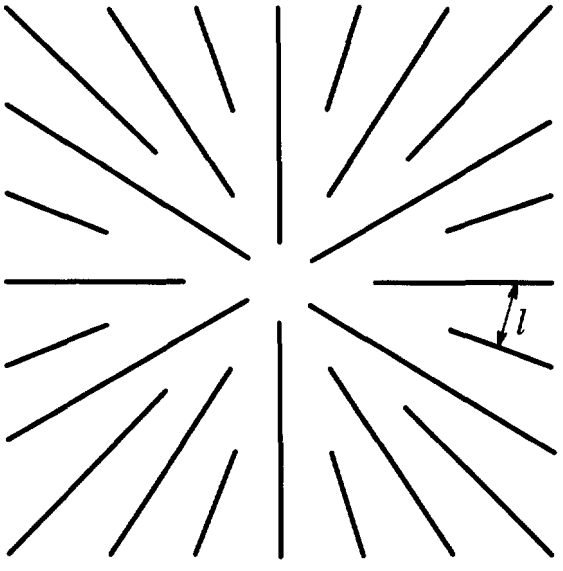

Fig. 10. Radial cracking pattern.

$$\dot{\chi} = \frac{J}{B} \geqslant 0 \tag{58}$$

where B is a kinetic coefficient. The rate-independent limit may be attained by letting $B \to 0$, which leads to the usual Kuhn–Tucker loading–unloading conditions

$$J \leqslant 0, \quad \dot{\chi} \geqslant 0, \quad J\dot{\chi} = 0. \tag{59}$$

A discretized form of the rate-independent kinetic relations is the energy balance equation

$$W(\varepsilon_{n+1}, \chi_n) - W(\varepsilon_{n+1}, \chi_{n+1}) = \frac{G_c}{l}(\chi_{n+1} - \chi_n) \tag{60}$$

which yields χ_{n+1} subject to the irreversibility condition $\chi_{n+1} > \chi_n$. This completes the definition of the model in the absence of plasticity.

In quasi-brittle materials, processes of elastic degradation and plasticity may operate simultaneously. The two mechanisms may be expected to be coupled in general. A simple model of elastoplastic coupling consists of formulating the laws of plasticity in terms of effective stresses and strains, σ^{eff} and ε^{eff} respectively (Ortiz and Popov, 1982). The resulting updates are also particularly simple. The given strains ε_{n+1} are first converted into effective strains using (45). A conventional elastic–plastic stress update, i.e., an update at fixed moduli, then follows. Finally, the resulting stresses and plastic strains are interpreted as effective values and the physical counterparts are computed through (44) and (45). Throughout these steps, the structure parameter is treated explicitly and held constant at χ_n. Following the stress update, the structure parameter can be updated by means of (60).

7.3. *Fracture time dependence*

The rate dependent character of the spall strength has been experimentally established for rocks (Grady and Kipp, 1979; Kipp *et al.*, 1980) and ceramics (Lankford, 1977, 1983). In these materials, the spall strength is found to be roughly proportional to a power of the strain rate. Within the framework of a cohesive fracture model, this effect can be investigated by considering a spall plane at $x = 0$ which is reached at $t = 0$ by an incident square pulse of magnitude σ^{in} and duration τ, Fig. 11. The corresponding incident velocity is given by

$$\sigma^{in} = -\rho c v^{in} \tag{61}$$

where c is the wave speed. Imagine that the spall plane is populated by a colinear array of

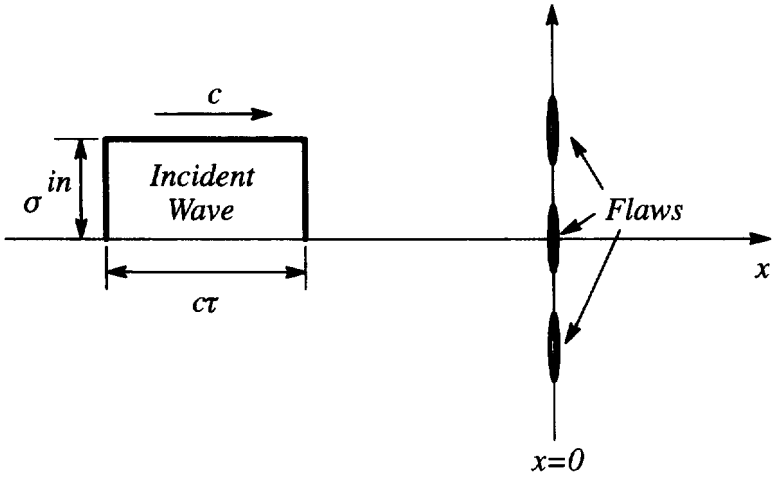

Fig. 11. Configuration for determining fracture time dependence.

flaws. If $\sigma^{in} > \sigma_{fr}$, the flaws grow and the resulting effective opening displacement δ is related to the stress acting on the spall plane through a cohesive law such as formulated in Section 7.1 (Ortiz, 1988). When the opening displacement reaches the critical value δ_{cr} the flaws coalesce and the spalling is complete.

When the incident wave impinges upon the spall plane, reflected and transmitted waves are induced of amplitudes

$$\sigma^{-} = \rho c v^{-} \tag{62}$$

$$\sigma^{+} = -\rho c v^{+} \tag{63}$$

where σ^{-}, v^{-} and σ^{+}, v^{+} are the stresses and particle velocities of the reflected and transmitted waves, respectively. Equilibrium across the spall plane requires

$$\sigma^{in} + \sigma^{-} = \sigma^{+}. \tag{64}$$

The cohesive law (32) with $\sigma_0 = \sigma_{fr}$ furnishes the additional relation

$$\sigma^{+} = \sigma_{fr}\left(1 - \frac{\delta}{\delta_{cr}}\right). \tag{65}$$

The opening velocity follows from compatibility as

$$\dot{\delta} = v^{+} - (v^{in} + v^{-}). \tag{66}$$

Equations (61–66) can be combined to obtain

$$\dot{\sigma}^{+} = \frac{2\sigma_{fr}}{\rho c\, \delta_{cr}}(\sigma^{+} - \sigma^{in}). \tag{67}$$

The solution of this equation for an initial value $\sigma^{+}(0) = \sigma_{fr} \leqslant \sigma^{in}$ is

$$\sigma^{+} = \sigma^{in} + (\sigma_{fr} - \sigma^{in})\mathrm{e}^{t/t_c} \tag{68}$$

where

$$t_c = \frac{\rho c\, \delta_{cr}}{2\sigma_{fr}} \tag{69}$$

is a characteristic relaxation time. From the conditions $\delta = \delta_{cr}$ or, equivalently, $\sigma^{+}(t_{fr}) = 0$, the time to spall t_{fr} follows in the form

$$t_{fr} = t_c \log \frac{\sigma^{in}}{\sigma^{in} - \sigma_{fr}}. \tag{70}$$

For a given pulse duration, τ, the incident stress amplitude σ^{in} needed for spall to occur is, therefore,

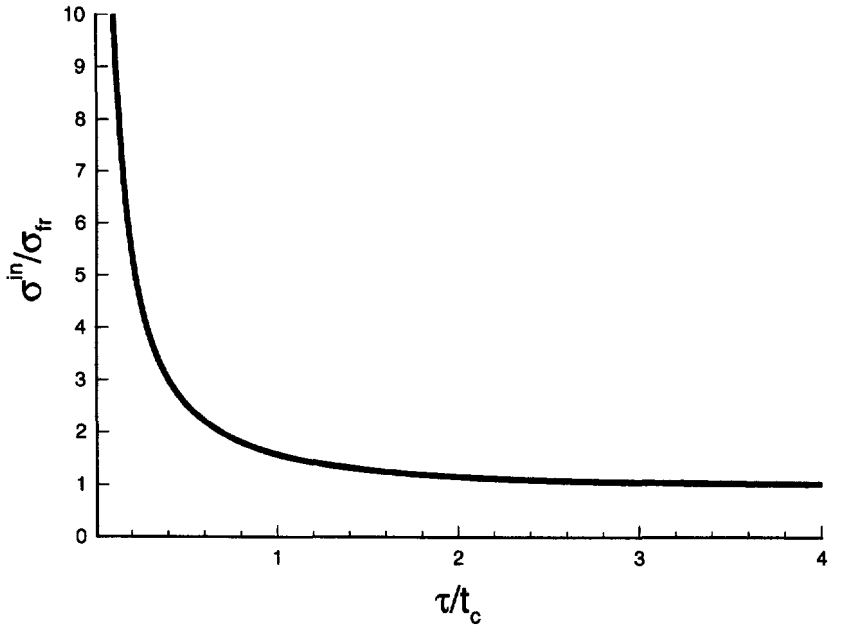

Fig. 12. Time dependence of the incident stress σ^{in} to cause fracture.

$$\sigma^{in} = \sigma_{fr}\frac{e^{\tau/t_c}}{e^{\tau/t_c}-1}. \tag{71}$$

This relation is shown in Fig. 12. Evidently, as the pulse duration decreases the pulse amplitude required to cause spall increases without bound. This effect results in an apparent spall strength enhancement at high rates of loading. Contrariwise, as the pulse duration increases, the pulse amplitude required to cause spall approaches asymptotically the quasi-static spall strength σ_{fr}.

8. DYNAMIC FRACTURE TESTS

8.1. *Spall tests*

As a first test of the model, we consider planar spall experiments such as performed by Grady and Kipp (1979) and Ahrens and Rubin (1993) to study the impact fracture properties of rock. For simplicity, we assume that the impactor–plate system deforms in uniaxial strain. This mode of deformation can conveniently be described by means of the simple axisymmetric meshes shown in Fig. 13. A steel impactor is assumed with a Young's modulus $E = 200$ GPa, a Poisson's ratio $\nu = 0.29$, a mass density $\rho = 7800$ kg/m^3, and a dilatational wave speed $c_d = 5797$ m/s. The impactor strikes an alumina plate with a Young's modulus $E = 260$ GPa, Poisson's ratio $\nu = 0.21$, mass density $\rho = 3690$ kg/m^3, fracture energy $G_c = 34$ J/m^2, a fracture stress $\sigma_{fr} = 400$ MPa, and dilatational wave speed $c_d = 8906$ m/s. The impactor strikes with an initial velocity of 30 m/s. The radial displacements are constrained on the outer radius of the mesh, which is set at 0.1 mm.

Figure 13a shows the fracture patterns obtained with a coarse mesh. Two main fractures at $X = 0.4$ mm to $X = 0.5$ mm develop in this case. By way of comparison, an elastic wave analysis predicts a spall plane to develop at $X = 0.46$ mm (Fig. 15). Therefore, the calculations match the location of the spall plane within the resolution of the mesh. The elastic analysis also shows that, owing to the higher impedance of the steel impactor, it remains in contact with the plate even after the tensile wave (that has been formed by the two interacting release waves) reaches the impactor–plate interface. Noticeably more fractures are created when a finer mesh is used in the calculations, Fig. 13b. This owes mainly to the presence of nearly transverse diagonal element sides, which fracture readily. The number of cracks is again reduced when the cohesive stresses are assumed to drop

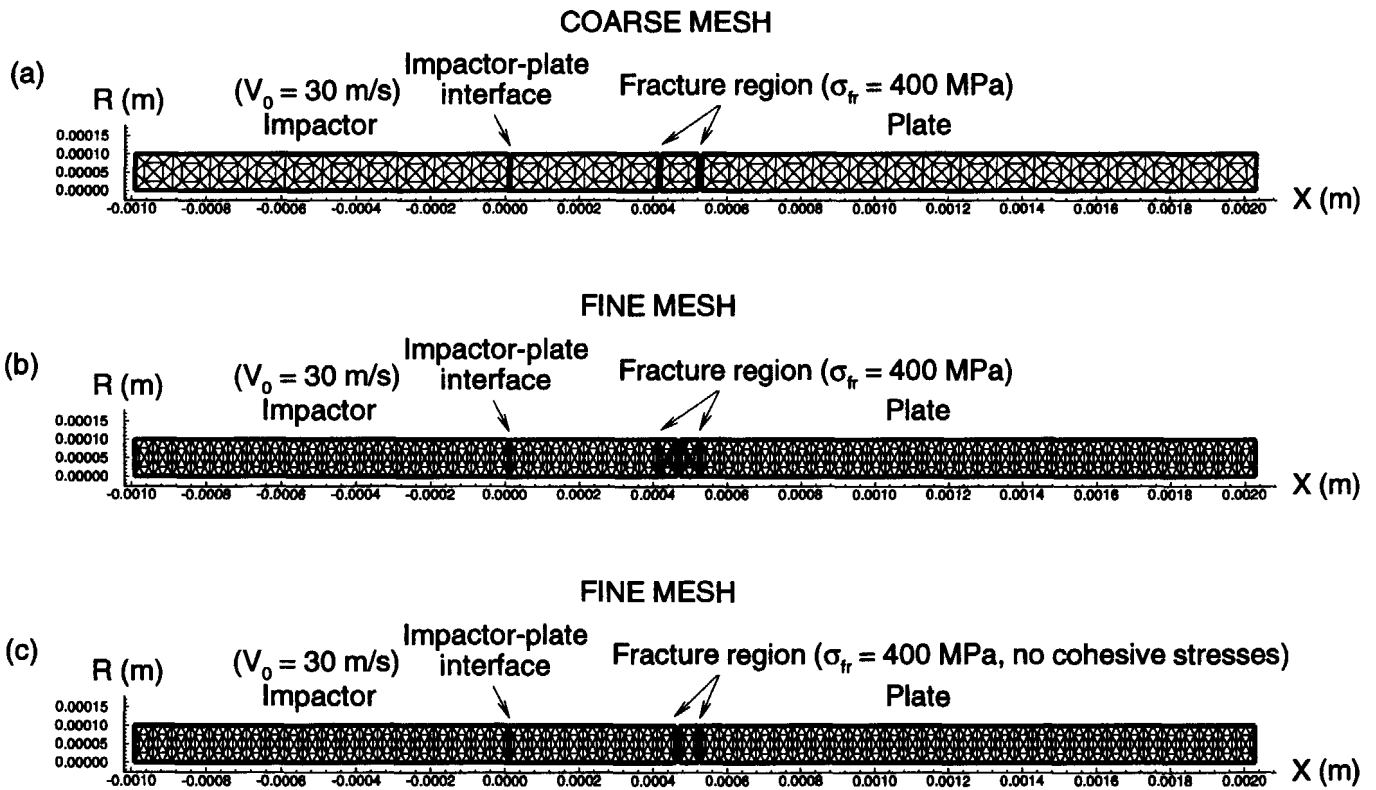

Fig. 13. Impactor–plate system: fractured configuration of coarse and fine meshes.

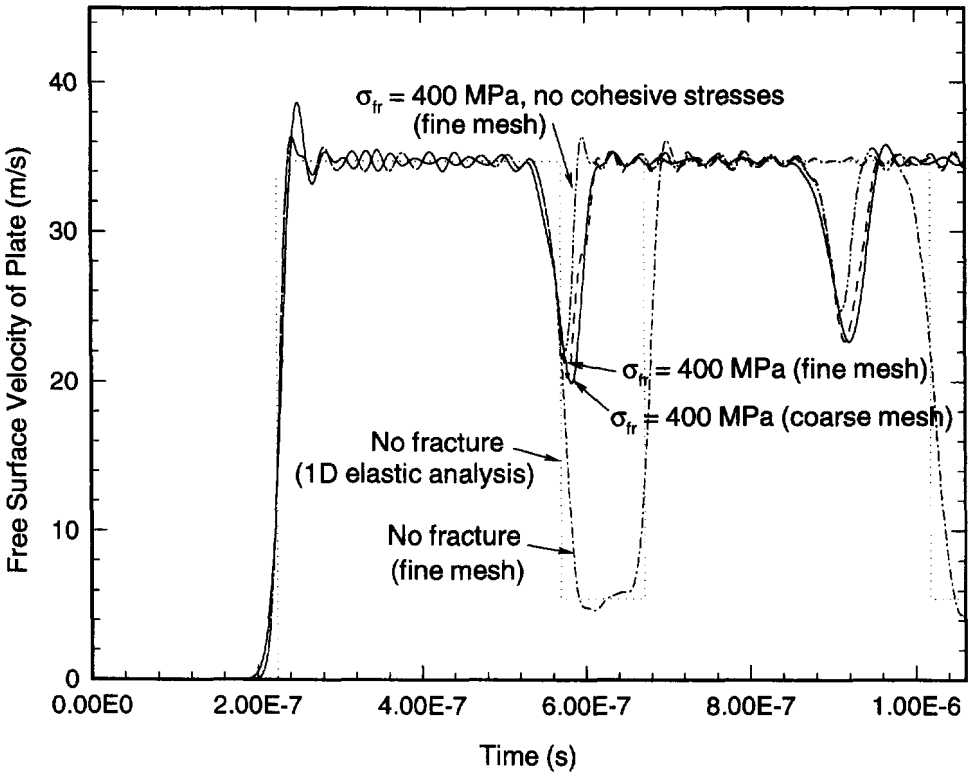

Fig. 14. Free surface velocity of plate for different cases.

suddenly to zero following the attainment of the fracture stress, Fig. 13c. In this case, unloading waves are induced at the fractures which tend to suppress further cracking in neighboring planes.

The particle velocity on the rear surface of the alumina plate is shown in Fig. 14. A purely elastic calculation is in fair agreement with the analytical solution derived from the $t-X$ and $\sigma-V$ diagrams shown in Figs 15 and 16, respectively. When fracture occurs, the rear surface velocity record takes the form of a pullback signal (Grady and Kipp, 1979), and the minimum velocity is markedly above the elastic value. Assuming vanishing cohesive stresses, the calculated pullback velocity is 22 m/s, which closely matches the elastic prediction of 20.66 m/s, Fig. 16. When cohesive stresses are taken into account, the calculated pullback velocity reduces to 20 m/s. This reduction reflects the nonvanishing work of separation expended at fractures.

8.2. *Double cantilever beam tests*

The double cantilever beam test (Kanninen, 1973, 1974; Hellan, 1978a, b; Kamath, 1987; Freund, 1990) provides an effective means of assessing the ability of the model to propagate cracks dynamically. We additionally use this test as a vehicle for investigating issues of mesh size dependency.

The specimen is loaded symmetrically in mode I, which enables the calculations to be restricted to one half of the specimen, Fig. 17. The specimen is assumed to deform in plane stress. The beam has a depth of 200 μm and an initial crack length of 400 μm. The specimen is extended to a length of 0.012 m so as to minimize wave reflections from the end. The material is an alumina of Young's modulus $E = 260$ GPa, a Poisson's ratio $\nu = 0.21$, a mass density $\rho = 3690$ kg/m^3, a fracture energy $G_c = 34$ J/m^2, a dilatational wave speed $c_d = 8906$ m/s, a shear wave speed $c_s = 5397$ m/s, and a Rayleigh wave speed $c_R = 4911$ m/s. For a Dugdale–Barrenblatt model I crack (Dugdale, 1960; Barrenblatt, 1962), in which the cohesive stress takes a constant value σ_{ave} up to a critical opening displacement

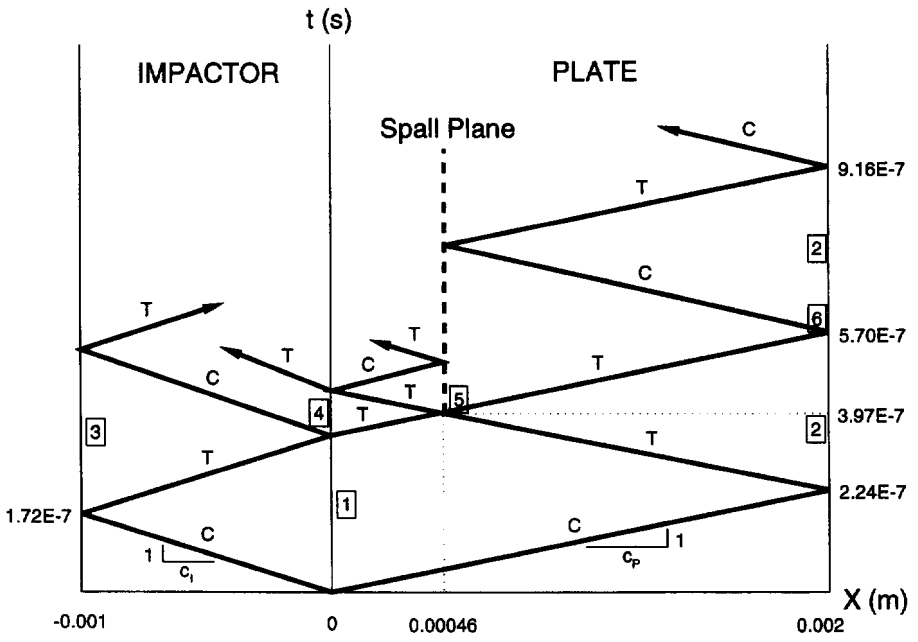

Fig. 15. Plate impact: Lagrangian t–X diagram.

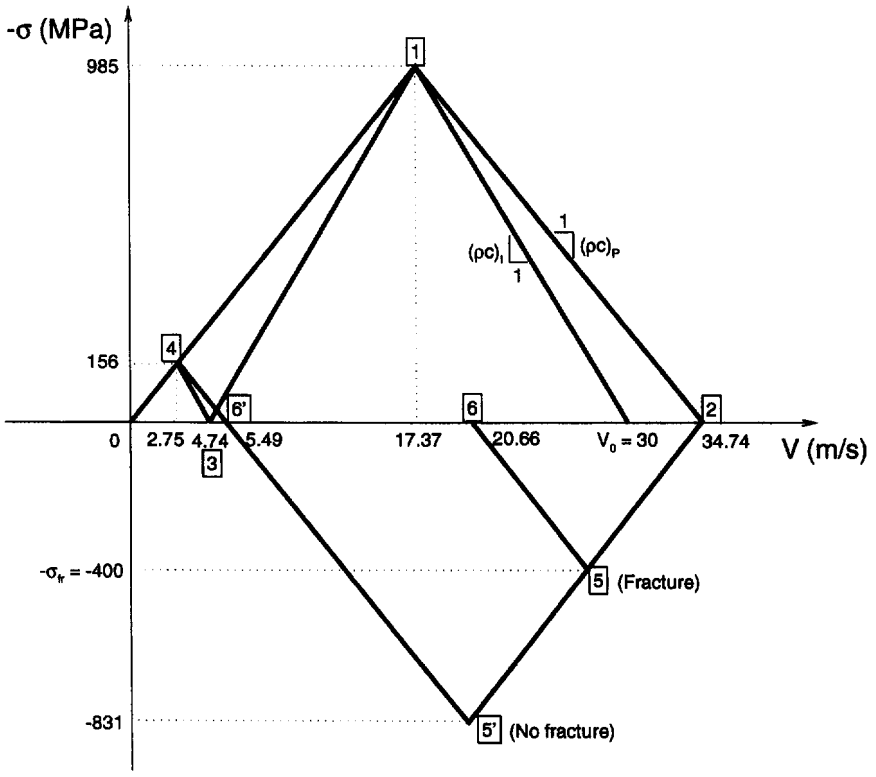

Fig. 16. Plate impact: stress–particle velocity diagram.

δ_{cr} and vanishes thenceforth, the size of the cohesive zone for quasistatic loading is (Rice, 1968):

$$R = \frac{\pi}{8}\frac{E}{1-\nu^2}\frac{G_c}{\sigma_{ave}^2}. \tag{72}$$

Inserting $\sigma_{ave} = \sigma_{fr}/2$ in this relation yields the estimate $R = 88$ μm. In calculations we use

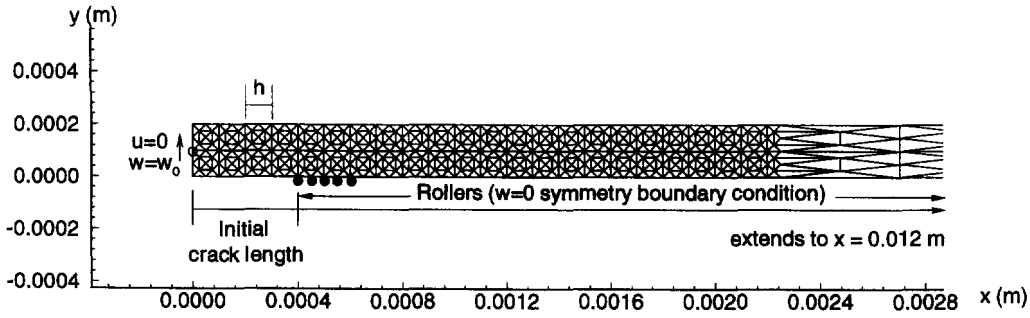

Fig. 17. Double cantilever beam : typical mesh.

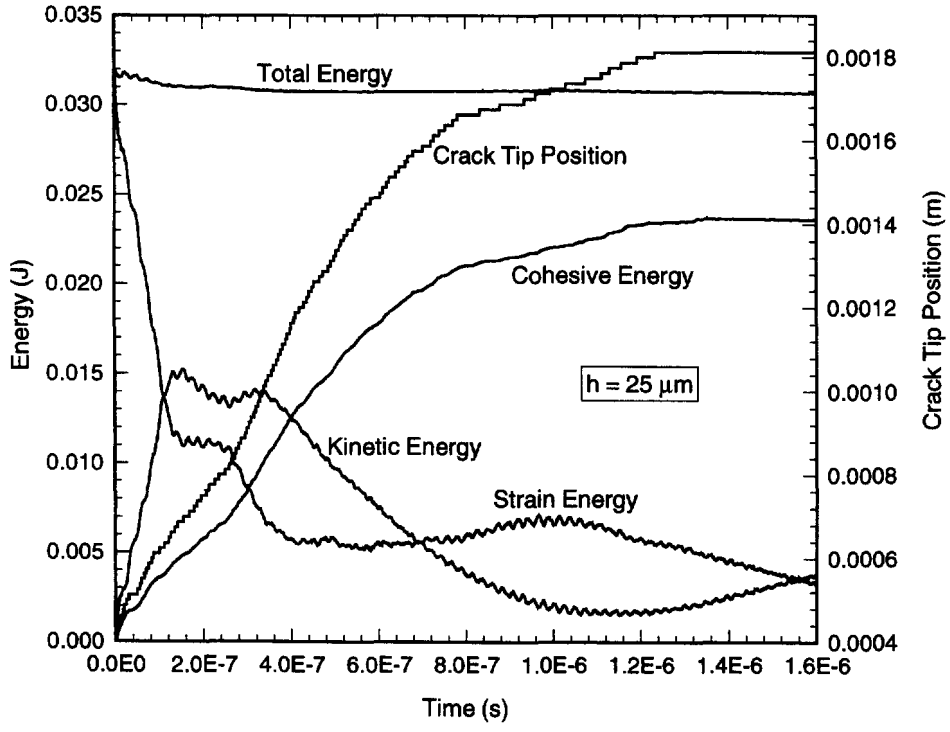

Fig. 18. Double cantilever beam : $h = 25$ μm and $w_0 = 4$ μm.

mesh sizes $h = 25, 50, 100, 200, 400$ μm. Evidently, the fine meshes resolve R, whereas the coarse ones do not. The analysis is conducted in two steps. Firstly, the beam tip is opened statically to $w_0 = 4$ μm. Secondly, the tip of the beam is held fixed and the crack is allowed to run dynamically in accordance with the cohesive law.

The crack tip position history for a mesh size $h = 25$ μm is shown in Fig. 18. Several stages of propagation can be discerned in the figure. During a first stage of 0.26 μs the crack propagates at a roughly constant speed of 1660 m/s, with a slight deceleration occurring at the end of the interval. Early in this stage, stress waves emitted from the crack tip traverse the depth of the beam and reflect from the free surface. After a few reverberations the continuum response is gradually replaced by beam-like behavior. In addition, shear waves travel from the initial crack tip to the fixed support at the tip of the beam and, upon reflection, catch up with the propagating crack tip and cause it to pause. The time of travel of the shear waves is approximately 0.24 μs. Hence, the arrival of the reflected shear wave to the crack tip signals the end of the first stage of propagation. It also follows that this transition is strongly dependent on the length and depth of the beam. The crack then accelerates up to an average speed of 1720 m/s in the interval $t = 0.26$–0.8 μs. As more of the initial energy stored in the beam is expended in the creation of new surface, the crack

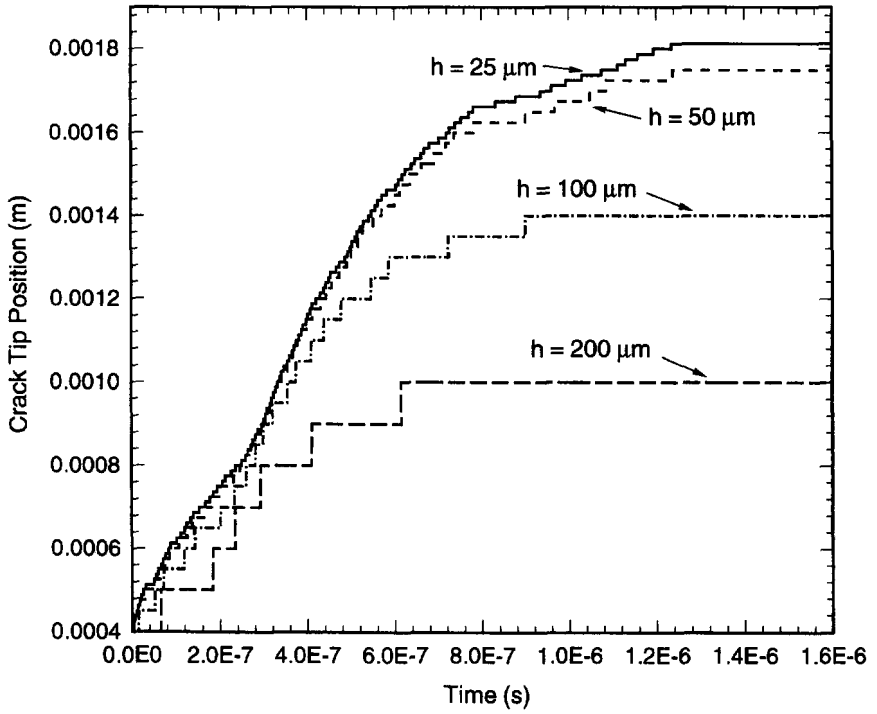

Fig. 19. Double cantilever beam: crack tip positions for meshes with $h = 25, 50, 100, 200$ μm and $w_0 = 4$ μm.

tip slows down considerably. Beyond $t = 0.8$ μs the crack tip velocity stays roughly constant at 300 m/s. Finally, the crack arrests at $t = 1.24$ μs.

Figure 18 also displays the history of strain, kinetic and cohesive energies. Initially, the strain energy dips sharply as it is transformed into kinetic energy. Following this initial transient, the strain and kinetic energies settle into a fairly sinusoidal variation reflecting the fundamental mode of vibration of the beam. The cohesive energy increases in direct proportion to the crack length and attains a maximum of 75% of the initial strain energy at crack arrest.

Figure 19 exhibits the effect of increasing mesh size on propagation. To facilitate comparison of results at different mesh sizes, we scale the wedging displacement w_0 so as to maintain constant the initial strain energy stored in the beam. The results for $h = 50$ μm and $h = 25$ μm are in fairly close agreement, which is suggestive of convergence with decreasing mesh size. As the mesh is coarsened to $h = 100$ and 200 μm, both of which exceed the characteristic cohesive zone size of 88 μm, the crack tip slows down markedly and arrests prematurely. For a mesh size $h = 400$ μm, the crack fails to propagate altogether, as the stress at the tip stays below the fracture stress at all times.

The effect of a higher initial strain energy is demonstrated by increasing the wedging displacement to $w_0 = 12$ μm, which results in a ninefold increase in strain energy. Figure 20 evidences the same early stages of propagation as in the previous case: a first stage with an average crack speed of 2200 m/s, followed by propagation at a fairly constant speed of 2300 m/s. These velocities correspond to nearly half the Rayleigh wave speed of $c_R = 4911$ m/s. The cohesive energy stays below 10% of the initial strain energy in the interval of time considered. In contrast to the lower energy calculation, however, the effect of mesh coarsening is now less severe, and the gross features of the crack tip motion are reproduced by the coarse mesh calculations, Fig. 21. It may therefore be concluded that the mesh dependency of the crack tip is lessened in situations in which the total energy driving the motion is greatly in excess of the cohesive energy required to fracture one additional element.

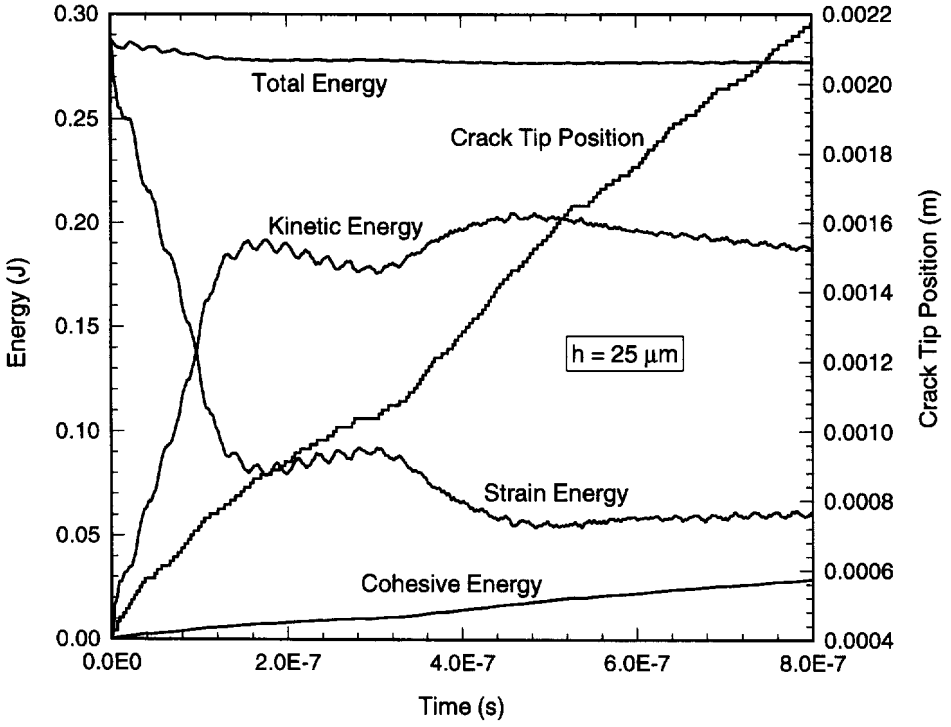

Fig. 20. Double cantilever beam : $h = 25$ μm and $w_0 = 12$ μm.

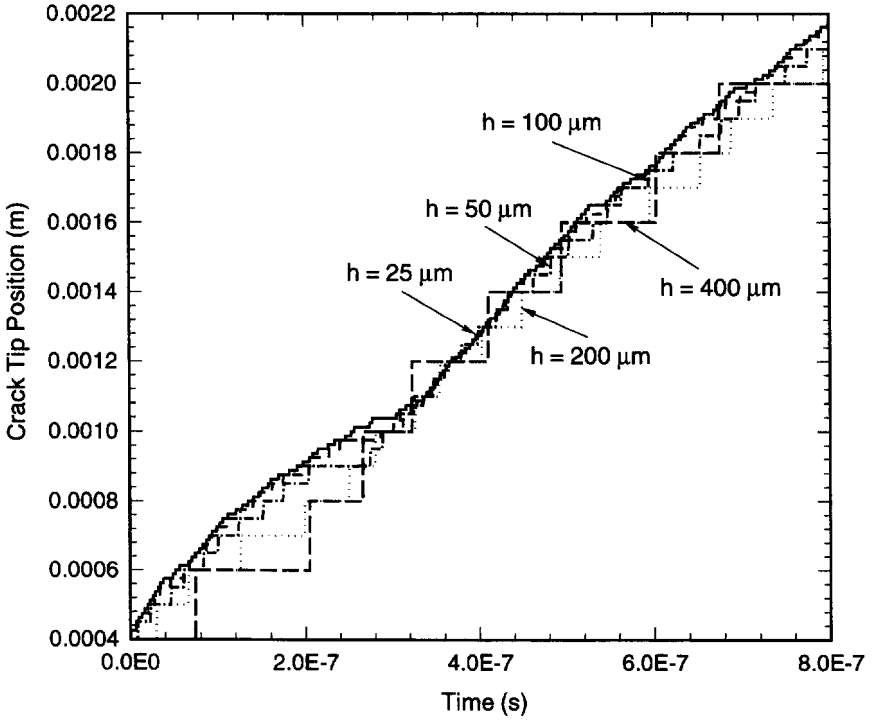

Fig. 21. Double cantilever beam : crack tip positions for meshes with $h = 25$, 50, 100, 200, 400 μm and $w_0 = 12$ μm.

9. PELLET IMPACT EXPERIMENTS

Ceramics are presently being evaluated as potential armor materials due to their high hardness and low density. Other properties of ceramics, such as their high melting point,

Table 1. Mechanical material constants

Material	ρ (kg/m^3)	E (GPa)	ν	σ_y (GPa)	m_1	m_2	n	$\dot{\varepsilon}_t$ (s^{-1})
Steel	7800	201	0.30	4.0	40	5	10	2×10^5
Alumina	3690	260	0.21	5.0	40	4	10	3×10^3

Table 2. Elastic wave speeds

Material	c_d (m/s)	c_s (m/s)	c_R (m/s)
Steel	5797	3100	2871
Alumina	8906	5397	4911

Table 3. Fracture material constants

Material	σ_{fr} (GPa)	G_c (J/m^2)	β_τ	μ	l (μm)
Steel	1.5	4074	0.0	0.25	100
Alumina	0.4	34	0.0	0.25	100

Table 4. Equation of state constants

Material	Γ	K_1 (GPa)	K_2 (GPa)	K_3 (GPa)
Steel	1.16	163.9	294.4	500.0
Alumina	1.0	149	149	0.0

Table 5. Thermal constants

Material	c (W/m/K)	k (J/kg/K)	α (/K)	T_0 (K)
Steel	477	38	0.00071	293
Alumina	795	26	0.00049	293

excellent wear and corrosion resistance make them attractive in certain structural applications such as turbine blades. In operation, the blades suffer frequent impacts by pellet-like objects and the resulting damage can limit the life of the component. In order to appraise the impact resistance of ceramics, Field (1988) shot pellets of a range of materials, including steel, tungsten carbide and lead, into ceramic and glass plates. Field examined the fracture patterns in the plate, which included large conical fragments, as well as the failure mechanisms in the pellets. In this section we apply the theory developed in the foregoing to the simulation of pellet impact experiments.

9.1. *Problem definition*

In order to have a direct comparison with observations, we consider one of Field's tests consisting of a 5 mm diameter hardened steel pellet impacting a Sintox alumina plate of 8.6 mm in thickness and 50 mm in diameter. The material properties of pellet and plate are collected in Tables 1–5. Due to the paucity of experimental measurements, we have had to estimate some of the constants from related material data found in the literature. A purely tensile failure criterion is adopted by setting $\beta_\tau = 0$ in the computation of the effective stress σ^{eff}. The distance l between potential meridional fracture planes is assumed to be 100 μm. An initial flaw size of 18 μm in the alumina yields a fracture stress of σ_{fr} of 400 MPa, and a fracture energy G_c of 34 J/m^2, both of which are in the range of observation (Grady, 1994). A friction coefficient μ of 0.25 is assumed between all contact surfaces.

The mesh size is set as $h = 250$ μm, which results in an initial mesh of 16,612 nodes and 8,146 elements. We start by meshing the domain by the advancing front method, which

results in fairly uniform element sizes. The corner nodes of the elements are then displaced in random directions and magnitudes of up to $h/2$, so as to introduce an element of randomness in the fracture process. A coarse model of mesh size $h = 360$ μm, comprising 7,494 nodes and 3,636 elements, is shown in Fig. 22. This coarse mesh is used for assessing the degree of mesh size dependency of the solution, as discussed subsequently. Simulations are conducted for impact velocities V_0 of 300 and 500 m/s, which are in the range of Field's experiments (Field, 1988). An intermediate impact velocity of $V_0 = 400$ m/s has been simulated (Camacho, 1996) but will not be reported here.

9.2. *Fracture patterns*

The calculated fracture evolution is shown in Figs 23 and 24. In the spirit of our axisymmetric model, we exhibit the meridional cracks explicitly and the radial cracks through level contours of the damage variable χ. Shortly after impact, surface flaws just outside the contact region grow into the interior of the plate driven by large tensile radial stresses. However, due to the rapidly expanding radius of contact between the pellet and the plate, these early surface cracks soon become subjected to predominantly compressive stresses and most of them arrest. Eventually, one surface crack continues its growth and develops into a conical crack with a well-defined semi-apex cone angle, henceforth simply termed cone angle. One or two additional extended conical cracks subsequently emanate from the leading edge of the spreading contact region. The occurrence of nested cone cracks has been consistently observed by Field (1988) in boron carbide plates. Tsai and Kolsky (1967) made similar observations in their steel pellet–glass plate impact experiments. The number of cone cracks increases with impact velocities due to the larger size attained by the contact region. The cone cracks propagate initially at fairly constant angles. As cone crack tips begin to interact with waves reflected from the rear surface of the plate the cone angle begins to increase. Eventually, the cone cracks reach the rear surface and conical fragments are detached from the plate. Conical fragments composed of single or double cones have indeed been recovered after impact by Field (1988).

In addition, radial damage spreads downward from the contact and eventually reaches the rear surface of the plate. The pattern of radial damage under the pellet approximates the median vent cracks which are observed to develop in impact or indentation tests (Evans and Wilshaw, 1977; Lawn and Wilshaw, 1975). Cylindrical cracks also develop early on near the axis and propagate downward from the contact. Similar cylindrical cracks propagate upward from the rear surface at later times driven by tensile bending stresses. To complete the pattern, lateral cracks initiate by branching from the cylindrical cracks. The growth of these cracks is promoted by reflected tensile waves and by relief waves following contact unloading. The resulting fracture pattern qualitatively agrees with the observations of Evans and co-workers (1977, 1978), Lawn and Wilshaw (1975) and Shockey *et al.* (1990b).

The pellet yields plastically and flattens at the contact with the plate, with maximum plastic strains of the order of 20% at 300 m/s and 60% at 500 m/s. Due to the pellet's brittleness, internal cracks initiate and propagate at roughly right angles to the principal tensile stresses. Eventually, axisymmetric fragments with heavy radial damage form due to the outward radial motion of the pellet. The extent of fragmentation of the pellet increases with the impact velocity, in keeping with Field's observations (1988) and the sphere fracture experiments of Arbiter *et al.* (1969).

9.3. *Effect of impact velocity*

As the impact velocity is increased, a larger number of cracks initiate and propagate into larger regions. In addition, the speed of propagation of the cracks increases. Thus, at $V_0 = 300$ m/s, the crack tip speed of the inner cone crack is in the order of 4000 m/s or 81% of the Rayleigh wave speed c_R, Fig. 23. At $V_0 = 500$ m/s, the same crack tip speed increases to 4600 m/s or 94% of c_R, Fig. 24, which approaches the theoretical limit. The outer cone cracks propagate more slowly than the inner cone cracks, and their propagation speed also increases with the impact velocity. Thus, the speed of the outer crack tip is in the order of 2900 m/s, or 59% of c_R, at $V_0 = 300$ m/s and 3300 m/s, or 67% of c_R, at $V_0 = 500$ m/s. These results are to be contrasted with the recent work of Strassburger and Senf (1994),

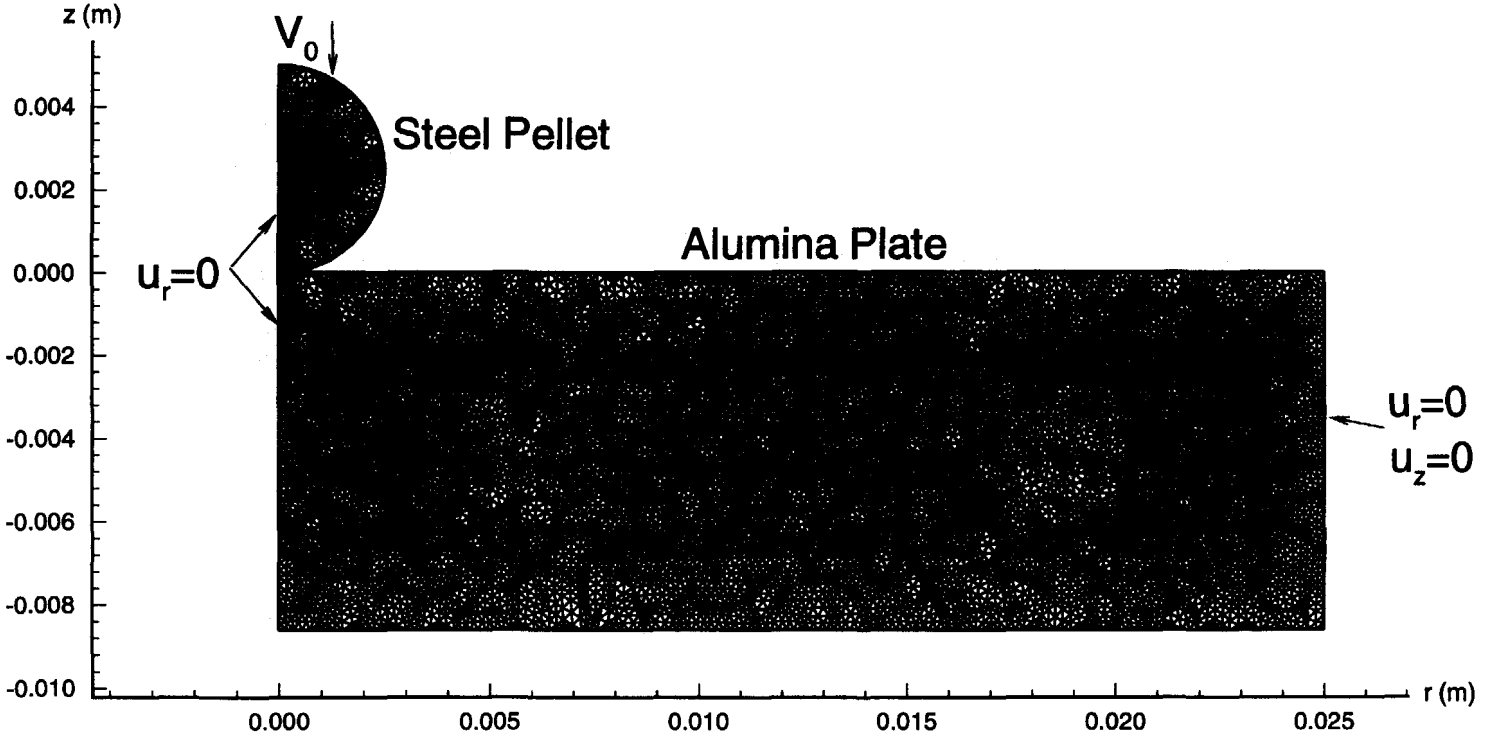

Fig. 22. Pellet and plate meshes, $h = 360\ \mu$m.

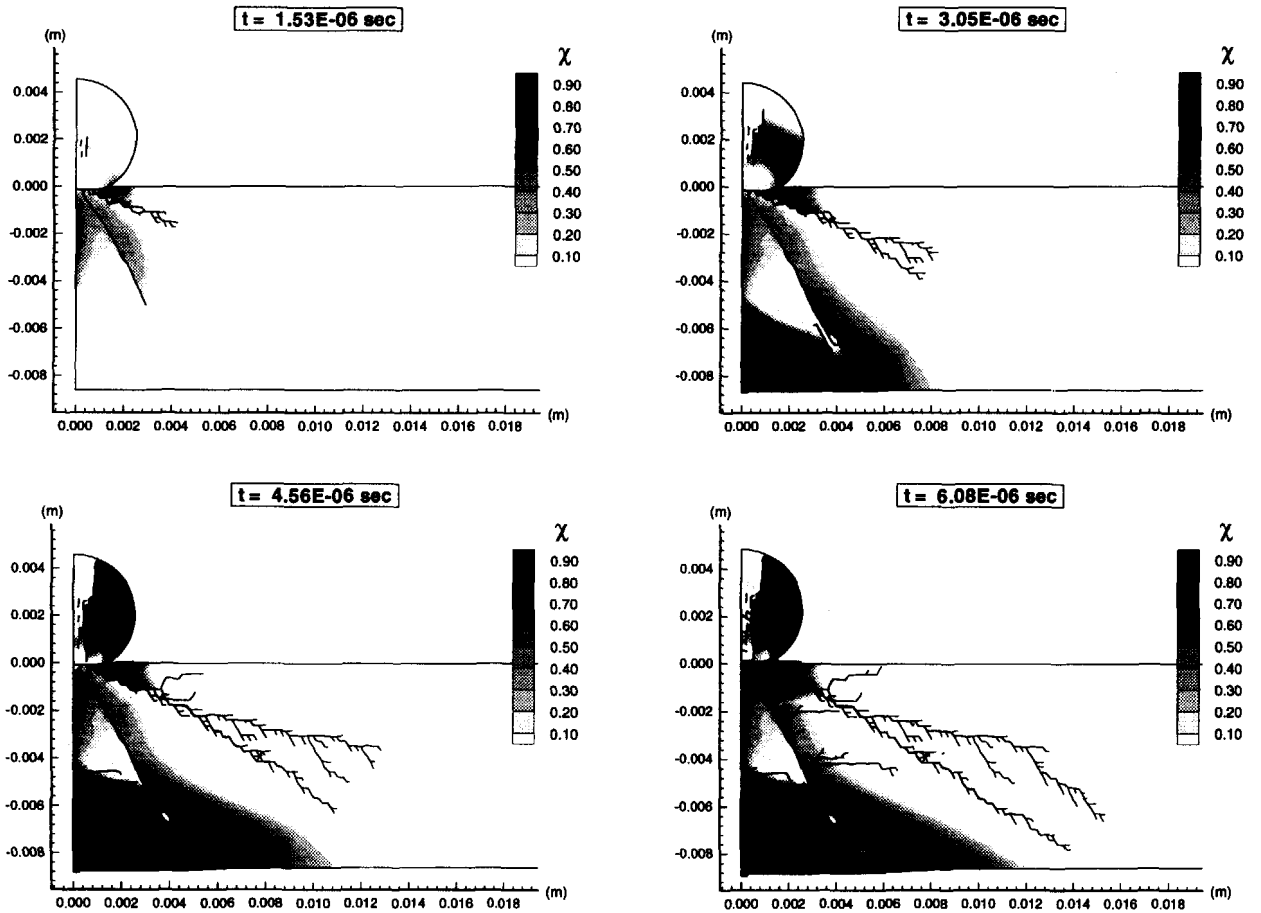

Fig. 23. Evolution of fracture patterns, $V_0 = 300$ m/s, $h = 250$ μm.

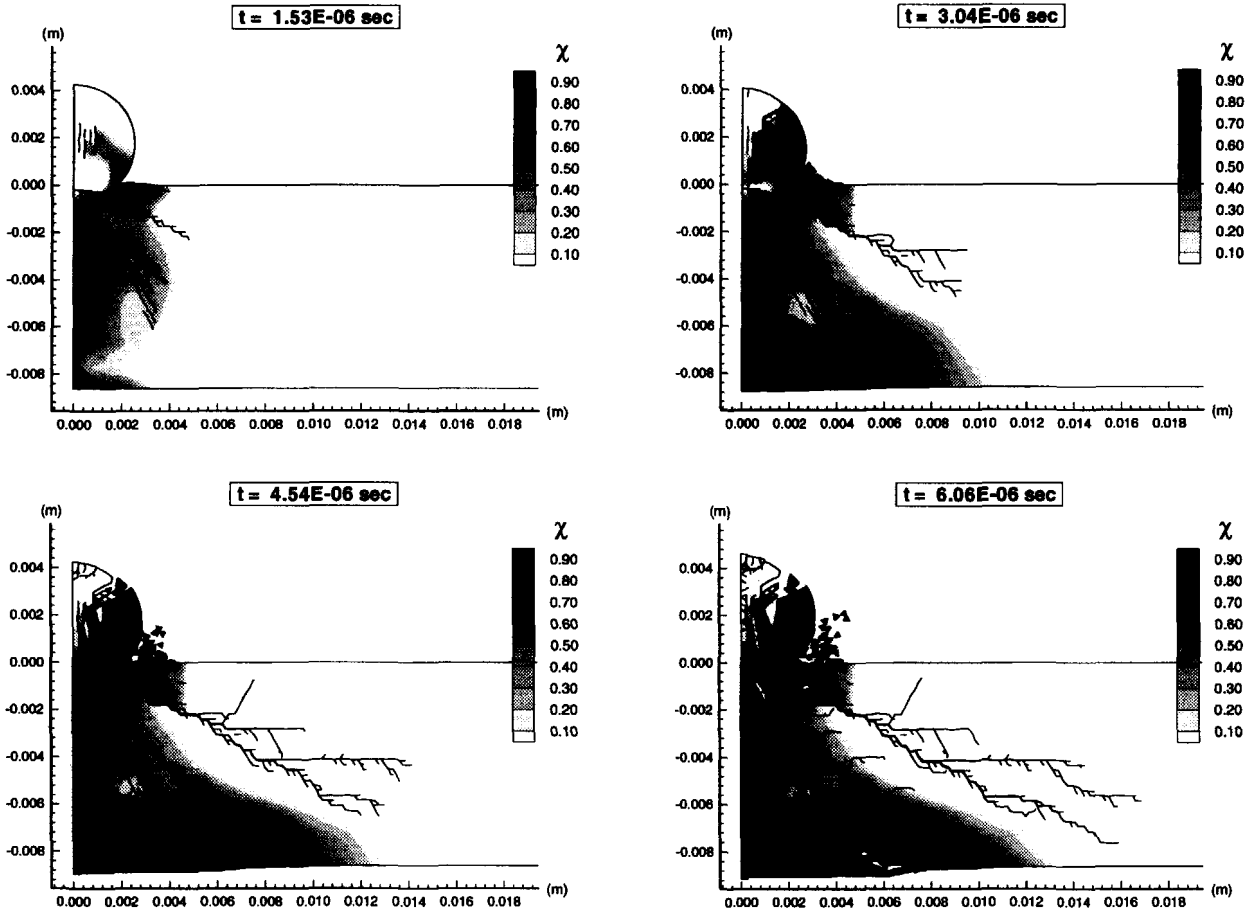

Fig. 24. Evolution of fracture patterns, $V_0 = 500$ m/s, $h = 250$ μm.

who have studied the relation between fracture and wave propagation in glass and ceramic tiles impacted edge-on by blunt cylindrical steel projectiles. Strassburger and Senf report damage velocities in alumina, e.g., propagation velocities of the fastest fracture observed or, alternatively, the mean velocity of a fracture front, approaching the dilatational wave speed for an impact velocity of 200 m/s, but these are subject to interpretation.

The extent of surface damage under the contact is noticeably larger for the impact velocity of $V_0 = 500$ m/s, Fig. 24. In particular, considerable fragmentation, including some ejecta at the edge of the contact region, takes place in this case. The calculated inner cone angle is sensitive to the impact velocity, while the outer cone angle remains close to the quasi-static value of approximately 64° independently of the impact velocity. At $V_0 = 300$ m/s, the initial inner cone angle is 32° and the base radius is 8 mm. At $V_0 = 500$ m/s, two inner cone cracks are observed at roughly 45° and a base radius of 11 mm. These results are in excellent agreement with the observations of Field (1988), who reports an average cone angle of 35° and a mean base radius of 8 mm at $V_0 = 300$ m/s, and a cone angle of 47° and a base radius of 13 mm at $V_0 = 500$ m/s. The development of conical cracks in ceramic plates under impact, and the increase of the cone angle with impact velocity, have the beneficial effect of spreading the load transmitted by the projectile (Wilkins, 1978; Field, 1988), in sharp contrast to metallic armor where the radius of the perforation is constant through the depth of the plate and comparable to the radius of the projectile.

9.4. *Effect of mesh size*

We have investigated the mesh-size sensitivity of the solution. Results for a mesh size of $h = 300$ μm are reported in Camacho (1996), which may be consulted for details. The solutions obtained on this mesh are essentially unchanged from those described in the foregoing for a mesh of $h = 250$ μm, which suggests a certain degree of convergence. It bears emphasis that a mesh size of 250 μm is not sufficient to resolve the quasistatic cohesive zone size of 88 μm in the ceramic plate. However, as demonstrated by the double cantilever beam tests of Section 8.2, good accuracy is still obtained under these conditions if sufficient strain energy is available to drive crack propagation. As shown in the following section, the cohesive energy expended in the creation of new surface is a small fraction of the energy input into the plate, which accounts for the limited mesh-size sensitivity up to $h = 300$ μm.

By way of contrast, considerable accuracy is lost when h is increased further to 360 μm. The solutions for $V_0 = 300$ and 500 m/s obtained from this coarse mesh are shown in Figs 25 and 26. At 300 m/s, mesh refinement is seen to result in a smooth and connected inner cone crack and increased branching of the outer cone cracks. Some of the branching which develops in the outer cone crack at 500 m/s is also suppressed in the coarse mesh solution. Cracks which undergo profuse branching and resemble a "fir tree branch" have been observed and classified by Strassburger and Senf (1994). Field (1988) in turn observed that the upper portion of the recovered inner cones has a relatively smooth surface, whereas the lower portion becomes increasingly rough due to stress wave interactions. It therefore appears that the coarse mesh size of 360 μm results in premature crack arrest leading to reduced branching of the outer cone crack and a disconnected inner cone crack.

Mesh refinement also partially suppresses the cracking and fragmentation near the axis. This effect is attributable to the development of a connected inner cone crack in the fine mesh solution, which relaxes more effectively the stress thus preventing extensive radial cracking from occurring. The progression of radial damage is somewhat retarded at early times by mesh refinement. Overall, however, the radial damage distribution is less sensitive to the mesh size than the discrete conical crack patterns.

9.5. *Stress fields*

Further insight into the failure mechanisms and their dependence on the impact velocity may be derived from an examination of the stress fields. Vector and contour plots of the principal stress more closely aligned with the circumferential direction are shown in Fig. 27. The remaining principal stresses are predominantly compressive and therefore do not contribute to fracture. In order to render the stress fields more readily interpretable, fracture

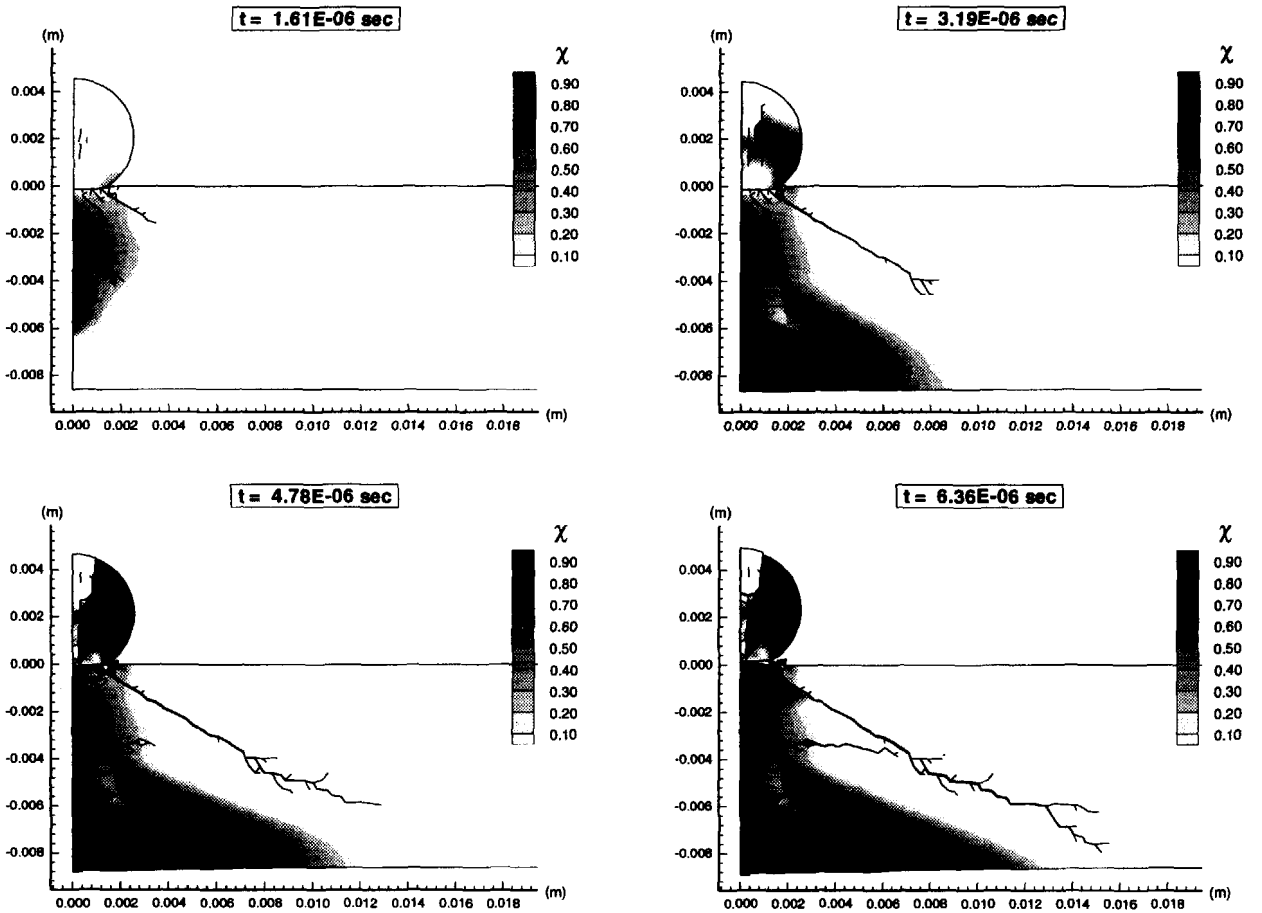

Fig. 25. Evolution of fracture patterns, $V_0 = 300$ m/s, $h = 360$ μm.

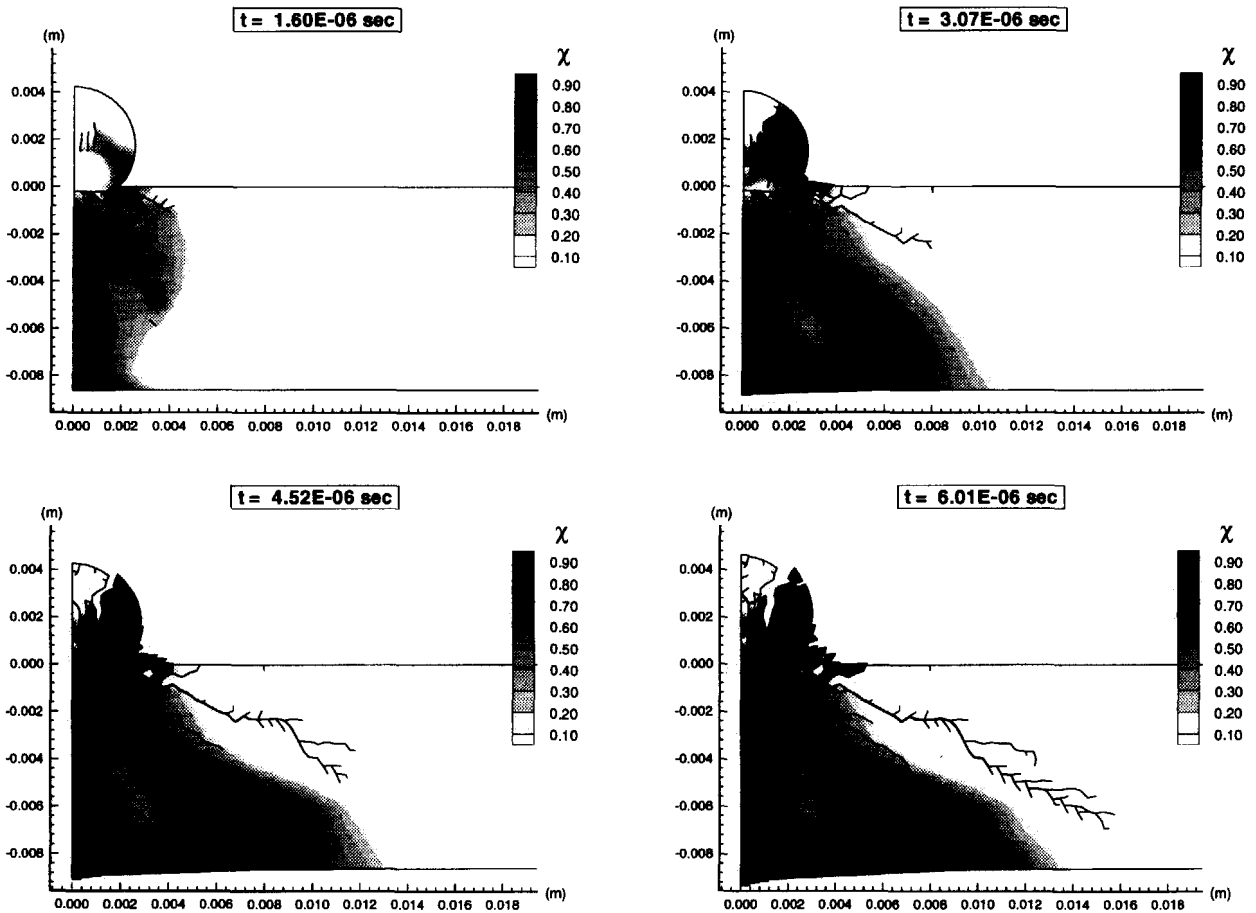

Fig. 26. Evolution of fracture patterns, $V_0 = 500$ m/s, $h = 360$ μm.

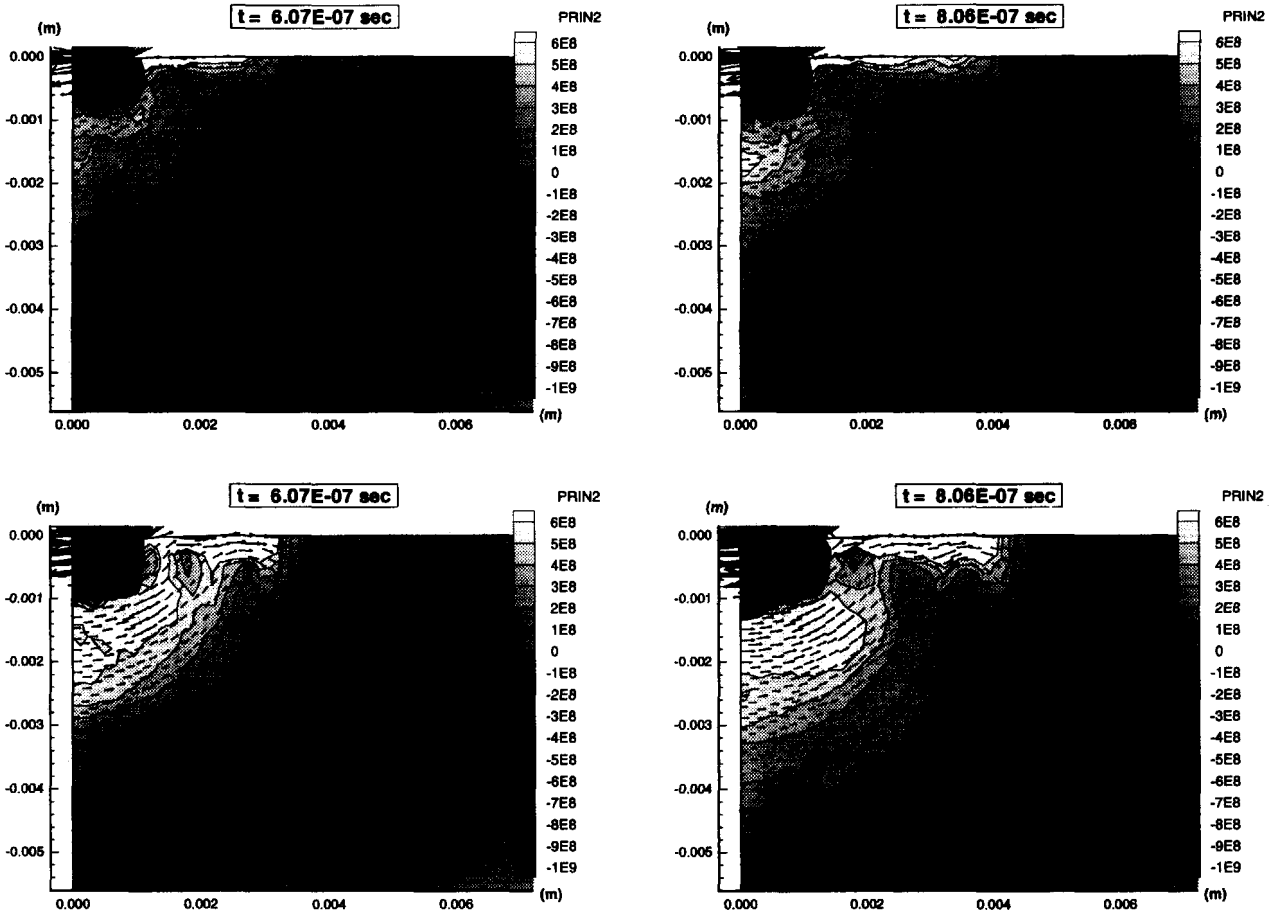

Fig. 27. Principal stress field : $V_0 = 300$ and 500 m/s, no fracture.

is not allowed for in these calculations. The elastic P, S and SP (head) waves induced by the pellet impact are superimposed on these plots for reference. It is observed that the principal stress is compressive near the P-wave front, changes to tensile within a sizeable annulus and becomes again compressive near the contact. It is evident from these fields that conical cracks initiate and propagate mainly in the tensile annular region. This is in keeping with the experiments of Fourney *et al.* (1975), in which circumferential tensile stresses radiating from a center of dilatation were found to be responsible for the initiation and propagation of circumferential cracks. It is also observed in Fig. 27 that the size and distance to the axis of the region of high tensile stresses increase with impact velocity. This in turn accounts for the tendency of the inner cone crack angle to increase with impact velocity.

Figure 28 shows the principal stress distributions which are obtained when fracture is allowed for. As expected, the magnitude of the tensile stresses is now noticeably lower. Nonetheless, the shift of the high tensile stress regions away from the axis with increasing impact velocity noted above, and the corresponding increase in cone crack angle, take place in the presence of fracture as well. It is also noteworthy that the fracture front in the 500 m/s case remains close to the S-wave front, which suggests a speed of propagation of the fracture front approaching the Rayleigh wave speed.

9.6. *Energy distribution*

The manner in which the kinetic energy supplied by the pellet is transferred into the system is of considerable interest. Figures 29 and 30 show the variation of kinetic energy, work of deformation, plastic work, and fracture energy, given in the expressions

$$K = \int_0^t \int_{B_0} \tfrac{1}{2}\rho_0 |\mathbf{v}|^2 \, \mathrm{d}V_0 \, \mathrm{d}t \tag{73}$$

$$W = \int_0^t \int_{B_0} \boldsymbol{\tau} : \mathbf{d} \, \mathrm{d}V_0 \, \mathrm{d}t \tag{74}$$

$$W^p = \int_0^t \int_{B_0} \bar{\sigma}\dot{\bar{\varepsilon}}^p \, \mathrm{d}V_0 \, \mathrm{d}t \tag{75}$$

$$\Gamma = \int_0^t \int_{\partial B_0} \mathbf{t}_{coh} \cdot \mathbf{v} \, \mathrm{d}S_0 \, \mathrm{d}t \tag{76}$$

where $\boldsymbol{\tau}$ is the Kirchhoff stress, $\bar{\sigma}$ is the equivalent Mises stress, $\dot{\bar{\varepsilon}}^p$ is the equivalent plastic strain rate and $\mathbf{t}_{coh}$ are the cohesive tractions. The minimum of the kinetic energy, the maximum in the work of deformation, and the saturation of the plastic work, occur simultaneously with the point of maximum indentation by the pellet.

Remarkably, despite the profuse cracking, the fracture energy amounts to an exceedingly small fraction, of the order of 1.5%, of the initial kinetic energy. By contrast, 44% of the initial kinetic energy at 300 m/s, and 50% at 500 m/s, is dissipated as plastic work, mostly in the steel pellet. The alumina plate experiences minimal plastic deformation primarily confined to a small region under the contact. The difference between the initial kinetic energy and the sum of the kinetic energy, work of deformation and fracture energy is the energy dissipated by friction. This energy is negligibly small at 300 m/s but amounts to a sizeable 10% of the initial kinetic energy at 500 m/s. The kinetic energy left in the system is 36% of the initial kinetic energy at 300 m/s, and 32% at 500 m/s. Evidently, this reduction is the result of increased inelastic dissipation at the higher impact velocity.

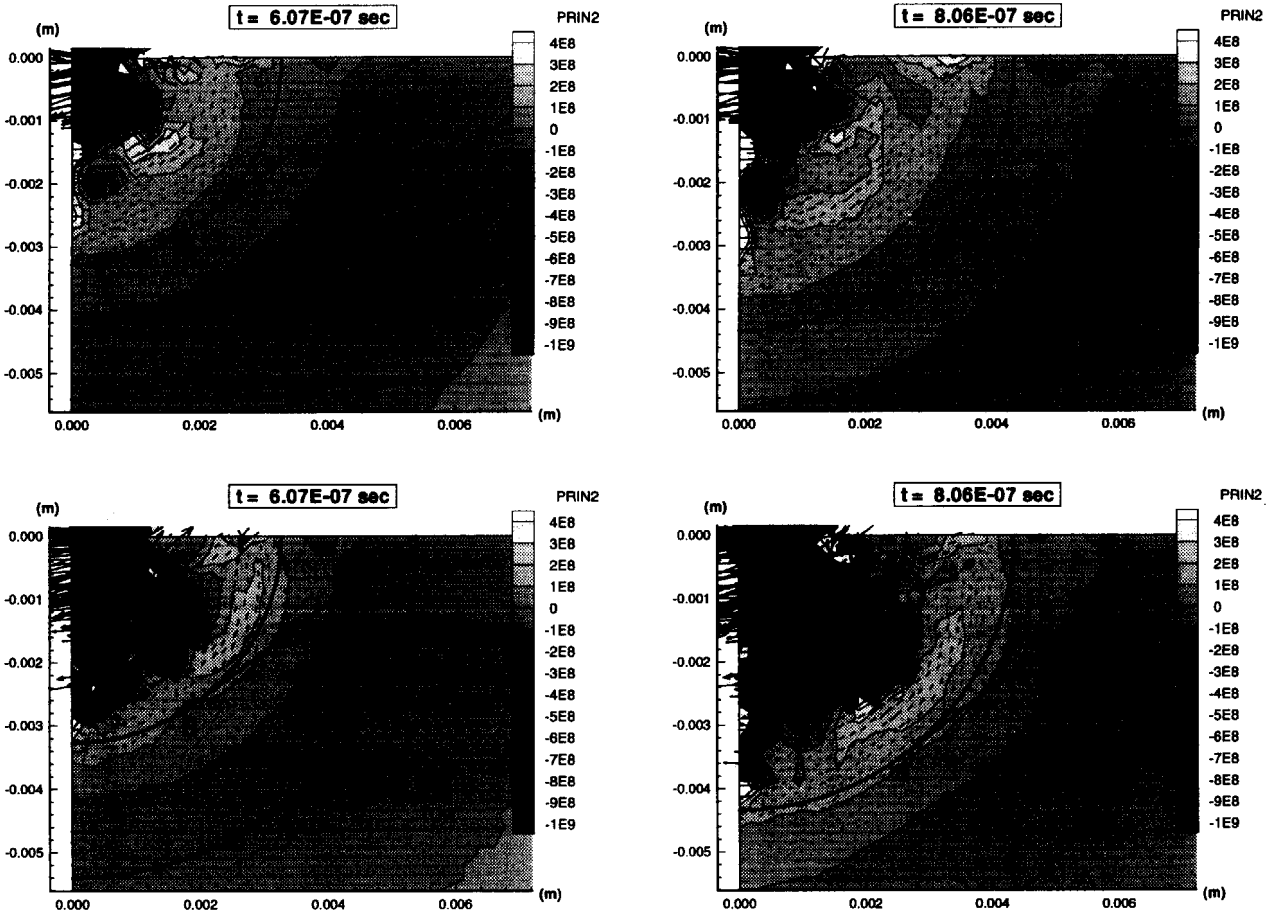

Fig. 28. Principal stress field : $V_0 = 300$ and 500 m/s, with fracture.

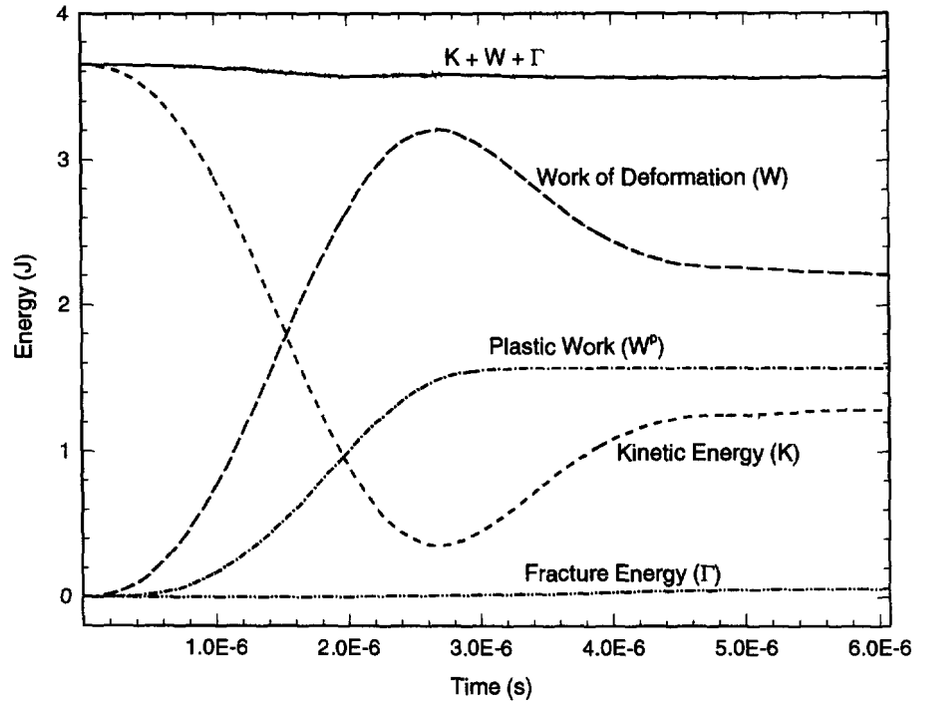

Fig. 29. Energy distribution: $V_0 = 300$ m/s, $h = 250$ μm.

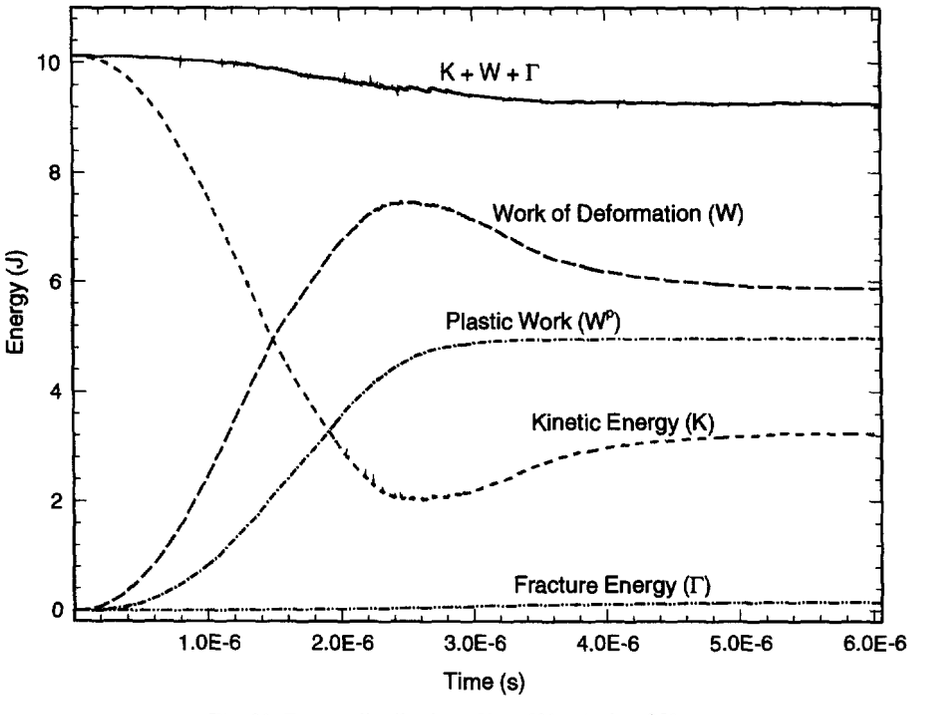

Fig. 30. Energy distribution: $V_0 = 500$ m/s, $h = 250$ μm.

10. SUMMARY AND DISCUSSION

We have developed a computational capability which enables detailed predictions of the progression of dynamic fracture and fragmentation in brittle materials subjected to impact. In a departure from past approaches to fragmentation, which treat the commuted phase as a homogeneized continuum, we follow the nucleation and propagation of discrete cracks by recourse to a cohesive fracture model. In axisymmetric calculations, however, we

account for radial cracking by a distributed damage model. The efficient enforcement of contact and friction between many bodies plays a key role in the capability. In particular, maintenance of a hierarchical system representation of the multi-bodies is essential for computational efficiency. Detailed comparisons with standarized dynamic fracture tests and with pellet–plate impact experiments demonstrate the power, versatility and predictive ability of the method.

Some of the limitations of the method should be carefully noted. The simulations presented are based on fixed meshes. This necessarily limits the number of available paths for fracture, possibly resulting in some biasing of the propagation directions. Because of the ability of the cracks to branch, however, paths which are not exactly coincident with mesh lines can be approximated as a jagged trajectory. This seems to alleviate the directional biasing to a considerable degree, as demonstrated by the good agreement of the calculated cone crack angles with Field's data (Field, 1988). Similar conclusions have been drawn by Xu and Needleman (1994). An additional shortcoming of working with a fixed mesh is that the initial elements in effect constitute the finest fragments which can be formed during the calculation.

These limitations can be overcome by recourse to adaptive meshing. By suitable local refinement at crack tips, the number of propagation directions available to the cracks can be substantially increased (Marusich and Ortiz, 1994). In addition, local refinement can be used to adequately resolve the crack tip fields, which may help to prevent premature crack arrest. One-element fragments can be remeshed into several elements, allowing the fragment to subdivide further (Camacho, 1966). This feature plays an important role in simulations of ballistic penetration of ceramic plates, which often result in a broad distribution of fragment sizes (Woodward *et al.*, 1994).

Acknowledgements—The work has been funded by the Army Research Office University Research Initiative through grant DAAL 03-92-G-0107. The authors are indebted to Profs R. Clifton, L. B. Freund and A. Bower of Brown University, to Prof. G. Ravichandran of the California Institute of Technology and to Drs J. Nagtegaal and D. Flanagan of HKS Inc. for helpful suggestions and discussions. The helpful comments and suggestions of the first reviewer are greatly appreciated.

REFERENCES

Ahrens, T. J., and Rubin, A. M. (1993). Impact-induced tensional failure in rock. *J. Geophys. Res.* **98,** 1185–1203.

Arbiter, N., Harris, C. C. and Stamboltzis, G. A. (1969). Single fracture of brittle spheres. *AIME Trans.* **244,** 118–133.

Baehmann, P. L., Wittchen, S. L., Shephard, M. S., Grice, K. R. and Yerry, M. A. (1987). Robust, geometrically-based, automatic two-dimensional mesh generation. *Int. J. Num. Meth. Engng* **24,** 1043–1078.

Barrenblatt, G. I. (1962). The mathematical theory of equilibrium of cracks in brittle fracture. *Adv. Appl. Mech.* **7,** 55–129.

Belytschko, T. (1983). An overview of semidiscretization and time integration procedures. In *Computational Methods for Transient Analysis* (Eds T. Belytschko and T. J. R. Hughes), North-Holland, Amsterdam, pp. 1–65.

Bowden, F. P. and Field, J. E. (1964). The brittle fracture of solids by liquid impact, by solid impact, and by shock. *Proc. R. Soc. Lond.* **A282,** 331–352.

Camacho, G. T. (1996). Computational modelling of impact damage and penetration of brittle and ductile solids. Ph.D. thesis, Brown University, Providence, R.I.

Cherepanov, G. P. and Sokokinsky, V. B. (1972). On fracturing of brittle bodies by impact. *Engng Fract. Mech.* **4,** 205–214.

Clifton, R. J. and Klopp, R. W. (1985). Pressure-shear plate impact testing. *Metals Handbook*, 9th edn, Vol. 8, 230–239.

Cuitiño, A. M. and Ortiz, M. (1992). A material-independent method for extending stress update algorithms from small-strain plasticity to finite plasticity with multiplicative kinematics. *Engng Comp.* **9,** 437–451.

Cundall, P. A. and Hart, R. D. (1992). Numerical modelling of discontinua. *Engng Comp.* **9,** 101–113.

Curran, D. R., Seaman, L. and Shockey, D. A. (1987). Dynamic failure of solids. *Phys. Rep.* **147,** 253–388.

Dienes, J. K. (1986). Comments on 'A generalized Griffith criteria for crack propagation'. *Engng Fract. Mech.* **23,** 615–617.

Dugdale, D. S. (1960). Yielding of steel sheets containing slits. *J. Mech. Phys. Solids* **8,** 100–104.

Espinosa, H. D., Raiser, G., Clifton, R. J. and Ortiz, M. (1992). Experimental observations and numerical modeling of inelasticity in dynamically loaded ceramics. *J. Hard Mat.* **3,** 285–313.

Evans, A. G. and Wilshaw, T. R. (1977). Dynamic solid particle damage in brittle materials : an appraisal. *J. Mat. Sci.* **12,** 97–116.

Evans, A. G., Gulden, M. E. and Rosenblatt, M. (1978). Impact damage in brittle materials in the elastic–plastic response regime. *Proc. R. Soc. Lond.* **A361,** 343–365.

Field, J. E. (1971). Brittle fracture : its study and application. *Contemp. Phys.* **12,** 1–31.

Field, J. E. (1988). Investigation of the impact performance of various glass and ceramic systems. USARDSG-UK ARO-E DAJA45-85-C-0021 Report. Cambridge University.
Fourney, W. L., Holloway, D. C. and Dally, J. W. (1975). Fracture initiation and propagation from a center of dilatation. *Int. J. Fract.* **11,** 1011–1029.
Freund, L. B. (1990). *Dynamic Fracture Mechanics.* Cambridge University Press, Cambridge.
Grady, D. E. and Kipp, M. E. (1979). The micromechanics of impact fracture of rock. *Int. J. Rock Mech. Min. Sci. & Geomech. Abstr.* **16,** 293–302.
Grady, D. E. and Kipp, M. E. (1993). Dynamic fracture and fragmentation. In *High-Pressure Shock Compression of Solids* (Eds J. R. Asay and M. Shahinpoor), Springer-Verlag, New York, pp. 265–322.
Grady, D. E. (1994). Dynamic failure of brittle solids. In *Fracture and Damage in Quasibrittle Structure* (Eds Z. P. Bazant, Z. Bittnar, M. Jirásec and J. Mazars) E. & FN Spon, pp. 259–272.
Hallquist, J. O., Goudreau, G. L. and Benson, D. J. (1985). Sliding interfaces with contact–impact in large-scale Lagrangian computations. *Comp. Meth. Appl. Mech. Engng* **51,** 107–137.
Hellan, K. (1978a). Debond dynamics of an elastic strip—I. Timoshenko beam properties and steady motion. *Int. J. Fract.* **14,** 91–100.
Hellan, K. (1978b). Debond dynamics of an elastic strip—II. Simple transient motion. *Int. J. Fract.* **14,** 173–184.
Hocking, G. (1992). The discrete element method for analysis of fragmentation of discontinua. *Engng Comp.* **9,** 145–155.
Hughes, T. J. R. and Belytschko, T. (1983). A précis of developments in computational methods for transient analysis. *J. Appl. Mech.* **50,** 1033–1041.
Hughes, T. J. R. (1983). Analysis of transient algorithms with particular reference to stability behavior. In *Computational Methods for Transient Analysis* (Eds T. Belytschko and T. J. R. Hughes), North-Holland, Amsterdam, pp. 67–155.
Jin, H. and Wiberg, N. E. (1990). Two-dimensional mesh generation, adaptive remeshing and refinement. *Int. J. Num. Meth. Engng* **29,** 1501–1526.
Johnson, G. R. and Holmquist, T. J. (1992). A computational constitutive model for brittle materials subjected to large strains, high strain rates, and high pressures. In *Shock-Wave and High-Strain Rate Phenomena in Materials* (Eds M. A. Meyers, L. E. Murr and K. P. Staudhammer), Marcel Dekker, New York, pp. 1075–1081.
Kachanov, L. M. (1986). *Introduction of Continuum Damage Mechanics.* Martinus Nijhoff Dordrecht, The Netherlands.
Kamath, S. M. (1987). Some aspects of the mechanics and mechanisms of dynamic brittle fracture. Ph.D. thesis, University of Illinois at Urbana-Champaign, University Microfilms International Order No. 8721673.
Kanninen, M. F. (1973). An augmented double cantilever beam model for studying crack propagation and arrest. *Int. J. Fract.* **9,** 83–91.
Kanninen, M. F. (1974). A dynamic analysis of unstable crack propagation and arrest in the DCB test specimen. *Int. J. Fract.* **10,** 415–430.
Kipp, M. E., Grady, D. E. and Chen, E. P. (1980). Strain-rate dependent fracture initiation. *Int. J. Fract.* **16,** 471–478.
Klopp, R. W., Clifton, R. J. and Shawki, T. G. (1985). Pressure–shear impact and the dynamic viscoplastic response of metals. *Mech. Mat.* **4,** 375–385.
Knight, C. G., Swain, M. V. and Chaudri, M. M. (1977). Impact of small steel spheres on glass surfaces. *J. Mat. Sci.* **12,** 1573–1586.
Kobayashi, S., Oh, S.-I. and Altan, T. (1989). *Metal Forming and the Finite Element Method.* Oxford University Press, Oxford.
Krajcinovic, D. and Lemaitre, J. (1987). *Continuum Damage Mechanics—Theory and Applications*, CISM Lectures, Springer Verlag, Berlin.
Lankford, J. (1977). Compressive strength and microplasticity in polycrystalline alumina. *J. Mat. Sci.* **12,** 791–796.
Lankford, J. (1983). The role of subcritical tensile microfracture processes in compression failure of ceramics. In *Fracture Mechanics of Ceramics*, Vol. 5 (Eds R. C. Bradt, A. G. Evans, D. P. H. Hasselman and F. F. Lange), Plenum Press, New York, pp. 625–637.
Lawn, B. R. and Wilshaw, T. R. (1975). Indentation fracture: principles and applications. *J. Mat. Sci.* **10,** 1049–1081.
Lemonds, J. and Needleman, A. (1986). Finite element analysis of shear localization in rate and temperature dependent solids. *Mech. Mat.* **5,** 339–361.
Lohner, R. (1988). Some useful data structures for the generation of unstructured grids. *Comm. Appl. Numer. Meth.* **4,** 123–135.
Longy, F. and Cagnoux, J. (1989). Plasticity and microcracking in shock-loaded alumina. *J. Am. Ceram. Soc.* **72,** 971–979.
Margolin, L. G. (1984). A generalized Griffith criterion for crack propagation. *Engng Fract. Mech.* **19,** 539–543.
Marusich, T. D. and Ortiz, M. (1995). Modelling and simulation of high-speed machining. *Int J. Num. Meth. Engng* **38,** 3675–3694.
Mathur, K. K., Needleman, A. and Tvergaard, V. (1993). Dynamic 3D analysis of the charpy V-notch test. *Model Simul. Mat. Sci. Engng* **1,** 467–484.
Ortiz, M. and Popov, E. P. (1982). A physical model for the inelasticity of concrete. *Proc. R. Soc. Lond.* **A383,** 101–125.
Ortiz, M. (1988). Microcrack coalescence and macroscopic crack growth initiation in brittle solids. *Int. J. Solids Structures* **25,** 231–250.
Ortiz, M. and Suresh, S. (1993). Statistical properties of residual stresses and intergranular fracture in ceramic materials. *J. Appl. Mech.* **60,** 77–84.
Park, K. C. and Felippa, C. A. (1983). Partitioned analysis of coupled systems. In *Computational Methods for Transient Analysis* (Eds T. Belytschko and T. J. R. Hughes), North-Holland, Amsterdam, pp. 157–219.
Peraire, J., Vahdati, M., Morgan, K. and Zienkiewicz, O. C. (1987). Adaptive remeshing for compressible flow computations. *J. Comp. Phys.* **72,** 449–466.
Rajendran, A. M. (1994). Modeling the impact behaviour of AD85 ceramic under multiaxial loading. *Int. J. Impact Engng* **15,** 749–768.
Rice, J. R. (1968). Mathematical analysis in the mechanics of fracture. In *Fracture*, Vol. 2 (Ed. H. Liebowitz), Academic Press, New York, pp. 191–311.

Seaman, L., Curran, D. R. and Murri, W. J. (1985). A continuum model for dynamic tensile microfracture and fragmentation. *J. Appl. Mech.* **52,** 593–600.
Shockey, D. A., Curran, D. R., Seaman, L., Rosenberg, J. T. and Petersen, C. F. (1974). Fragmentation of rock under dynamic loads. *Int. J. Rock Mech. Min. Sci. & Geomech. Abs.* **11,** 303–317.
Shockey, D. A., Marchand, A. H., Skaggs, S. R., Cort, G. E., Burkett, M. W. and Parker, R. (1990a). Failure phenomenology of confined ceramic targets and impacting rods. *Int. J. Impact Engng* **9,** 263–275.
Shockey, D. A., Rowcliffe, D. J., Dao, K. C., and Seaman, L. (1990b). Particle impact damage in silicon nitride. *J. Am. Ceram. Soc.* **73,** 1613–1619.
Steinberg, D. J. (1991). Computer studies of the dynamic strength of ceramics. *J. Physique IV*, 837–844.
Strassburger, E. and Senf, H. (1994). Experimental investigation of wave and fracture phenomena in impacted ceramics. Ernst-Mach-Institut, Germany.
Taylor, G. I. and Quinney, H. (1931). The plastic distortion of metals. *Philos. Trans. Roy. Soc. London* **A230,** 323–362.
Taylor, L. and Flanagan, D. (1987). PRONTO 2D: a two-dimensional transient solid dynamics program. *SAND*86-0584, Sandia National Laboratories, Albuquerque, NM.
Tsai, Y. M. and Kolksy, H. (1967). A study of the fractures produced in glass blocks by impact. *J. Mech. Phys. Solids* **15,** 263–278.
Walter, J. (Ed.) (1992). Material modeling for terminal ballistic simulation. Technical Report BRL-TR-3392, U.S. Army Ballistic Research Laboratory, Maryland.
Wilkins, M. L. (1978). Mechanics of penetration and perforation. *Int. J. Engng Sci.* **16,** 793–807.
Woodward, R. L., Gooch, W. A., O'Donnell, R. G., Perciballi, W. J., Baxter, B. J. and Pattie, S. D. (1994). A study of fragmentation in the ballistic impact of ceramics. *Int. J. Impact Engng* **15,** 605–618.
Xu, X.-P. and Needleman, A. (1994). Numerical simulations of fast crack growth in brittle solids. *J. Mech. Phys. Solids* **42,** 1397–1434.
Zhong, Z. H. and Nilsson, L. (1990). A contact searching algorithm for general contact problems. *Comp. & Struct.* **33,** 197–209.
Zhou, M., Clifton, R. J. and Needleman, A. (1992). Shear band formation in a W-Ni-Fe alloy under plate impact. In *Tungsten & Tungsten Alloys*—1992, Metal Powder Industries Federation, Princeton, N.J.

APPENDIX A. CONSISTENT COMPUTATION OF NODAL TRACTIONS

Let Γ be an oriented internal boundary of the mesh. Let s denote the arc-length measured along Γ. Let $\mathbf{n}(s)$ be the exterior unit normal to Γ. The distribution $\mathbf{t}(s)$ of tractions on Γ is discretized in the form

$$t_i(s) = \sum_{a \text{ on } \Gamma} t_{ia} N_a(s) \tag{A1}$$

where $\mathbf{t}_a$ are the nodal tractions and $N_a(s)$ is the restriction of the global shape function N_a to Γ. To determine $\mathbf{t}_a$ multiply (A1) by $N_a(s)$ and integrate over Γ to obtain

$$\sum_{a \text{ on } \Gamma} w_{ba} t_{ia} = \int_\Gamma t_i(s) N_b(s)\, \mathrm{d}s \tag{A2}$$

where

$$w_{ab} = \int_\Gamma N_a(s) N_b(s)\, \mathrm{d}s \tag{A3}$$

are coefficients with units of length. The right hand side of (A2) can be evaluated by writing $t_i = \sigma_{ij} n_j$, where σ_{ij} are the components of the Cauchy stress tensor, and integrating by parts, with the result

$$\int_\Gamma t_i(s) N_b(s)\, \mathrm{d}s = \sum_{e \text{ adj. } \Gamma} \left[m_b^e a_{ib} - \int_{\Omega^e} B^e_{jkb} \sigma_{jk}\, \mathrm{d}\Omega^e \right] \equiv f_{ib} \tag{A4}$$

where m_b^e is the lumped mass of node b contributed by element e and the sum extends to all elements e adjacent to Γ and $\mathbf{B}_a^e$ is the usual B-matrix. Note that we consider only the elements on the side of Γ. It should also be carefully noted that, owing to mass lumping, inertia forces contribute directly to the balance of linear momentum of the surface. Solving (A2) gives

$$t_{ia} = \sum_{b \text{ on } \Gamma} m_{ab}^{-1} f_{ib}. \tag{A5}$$

Again, it should be carefully noted that the forces $\mathbf{f}_a$ are to be assembled from elements lying on one side of Γ only (the other side can be treated likewise). The inversion of w_{ab} can be provided by recourse to lumping. Let

$$w_a = \sum_b w_{ab} \tag{A6}$$

Then (A5) can be replaced by

$$t_{ia} = \frac{f_{ia}}{w_a}. \tag{A7}$$

The weights w_a may be interpreted as the length of Γ tributary to node a.